AD_____

Award Number: DAMD17-98-1-8148

TITLE: Development of Quantitative Microvascular Breast MRI

PRINCIPAL INVESTIGATOR: Brian Rutt, Ph.D.

CONTRACTING ORGANIZATION: John P. Robarts Research Institute
London, Ontario, Canada N6A 5K8

REPORT DATE: July 2000

TYPE OF REPORT: Annual

PREPARED FOR: U.S. Army Medical Research and Materiel Command
Fort Detrick, Maryland 21702-5012

REPORT DOCUMENTATION PAGE

Form Approved
OMB No. 074-0188

1. AGENCY USE ONLY (Leave blank)	2. REPORT DATE	3. REPORT TYPE AND DATES COVERED
	July 2000	Annual (1 Jul 99 - 30 Jun 00)

4. TITLE AND SUBTITLE
Development of Quantitative Microvascular Breast MRI

5. FUNDING NUMBERS
DAMD17-98-1-8148

6. AUTHOR(S)
Brian Rutt, Ph.D.

7. PERFORMING ORGANIZATION NAME(S) AND ADDRESS(ES)
John P. Robarts Research Institute
London, Ontario, Canada N6A 5K8

E-MAIL:
brutt@irus.rri.on.ca

8. PERFORMING ORGANIZATION REPORT NUMBER

9. SPONSORING / MONITORING AGENCY NAME(S) AND ADDRESS(ES)
U.S. Army Medical Research and Materiel Command
Fort Detrick, Maryland 21702-5012

10. SPONSORING / MONITORING AGENCY REPORT NUMBER

11. SUPPLEMENTARY NOTES

12a. DISTRIBUTION / AVAILABILITY STATEMENT
Approved for public release; distribution unlimited

12b. DISTRIBUTION CODE

13. ABSTRACT ***(Maximum 200 Words)***

The purpose of this research is to develop a non-invasive predictor of malignancy in breast tumours through the design and preliminary validation of a new form of magnetic resonance imaging (MRI). The hypothesis is that the spatial distribution of microvasculature around a solid breast lesion is specific for malignancy and can be reliably measured at high resolution by a completely non-invasive, non-contrast-enhanced MRI method. This is being tested by achieving the following:

1. Design/building/testing of ultra-high-strength gradient coils for human breast imaging at 1.5 Tesla (T) and 4T.
2. Design/implementation/testing of MR pulse sequences for selective mapping of microvascular parameters.
3. Correlation of MR-derived microvascular parameters with true microvessel density in a rat model of human breast cancer.

A gradient coil has been designed that is suitable for high resolution imaging of tumours in rats and achieves gradient strengths up to 300mT/m (typical clinical systems achieve 40mT/m). A non-contrast-enhanced MRI pulse sequence that uses diffusion weighting has been implemented at 1.5T, and has been used to acquire images of breast tumours in rats. Using an analysis program designed in house, our preliminary results show that our technique allows imaging of the micravasculature in tumours.

The significance of this research is that, with relatively low-cost modifications to MR imaging equipment, it should be possible to detect, diagnose, and provide much improved prognosis of lesions suspected to be breast cancer. Further, this technique will measure non-invasively the microvasculature, allowing monitoring of anti-angiogenic treatments.

14. SUBJECT TERMS
Breast Cancer, tumour angiogenesis, microvessel density, high Strength gardient coils, high field MRI diagnosis

15. NUMBER OF PAGES
75

16. PRICE CODE

17. SECURITY CLASSIFICATION OF REPORT	18. SECURITY CLASSIFICATION OF THIS PAGE	19. SECURITY CLASSIFICATION OF ABSTRACT	20. LIMITATION OF ABSTRACT
Unclassified	Unclassified	Unclassified	Unlimited

FOREWORD

Opinions, interpretations, conclusions and recommendations are those of the author and are not necessarily endorsed by the U.S. Army.

___ Where copyrighted material is quoted, permission has been obtained to use such material.

___ Where material from documents designated for limited distribution is quoted, permission has been obtained to use the material.

___ Citations of commercial organizations and trade names in this report do not constitute an official Department of Army endorsement or approval of the products or services of these organizations.

X In conducting research using animals, the investigator(s) adhered to the "Guide for the Care and Use of Laboratory Animals," prepared by the Committee on Care and use of Laboratory Animals of the Institute of Laboratory Resources, national Research Council (NIH Publication No. 86-23, Revised 1985).

N/A For the protection of human subjects, the investigator(s) adhered to policies of applicable Federal Law 45 CFR 46.

N/A In conducting research utilizing recombinant DNA technology, the investigator(s) adhered to current guidelines promulgated by the National Institutes of Health.

N/A In the conduct of research utilizing recombinant DNA, the investigator(s) adhered to the NIH Guidelines for Research Involving Recombinant DNA Molecules.

N/A In the conduct of research involving hazardous organisms, the investigator(s) adhered to the CDC-NIH Guide for Biosafety in Microbiological and Biomedical Laboratories.

JULY 6 2000

PI - Signature Date

Table of Contents

Introduction

X-ray mammography is currently the clinically accepted modality for breast cancer screening. Mammography, however, is particularly unreliable and recent trials have shown that 70-80% of mammographically indeterminate lesions that progress to surgical biopsy are benign.[1-4] Development of an accurate, non-invasive imaging test with low false negative rates would allow reduction of the two step process of surgical biopsy followed by surgical lesion removal to a single step, as well as providing a tool for guiding treatment decisions. It may be possible to achieve this through the development of a non-invasive technique that measures microvessel density. Tumour progression is known to be dependent on the ability to stimulate the growth of new blood vessels that supply nutrients and oxygen to the expanding tumour. Based on recent studies that indicate that the onset of angiogenesis can occur before a tumour reaches its maximum diffusion-limited growth potential(1-2 mm diameter) and may occur well before the switch to a malignant phenotype,[5-15] it has been hypothesized that the characteristic new vessel growth associated with tumour angiogenesis should allow differentiation between malignant and benign breast lesions.[16-21] The purpose of this research is to develop a non-invasive predictor of malignancy through the design and preliminary validation of a new form of magnetic resonance imaging (MRI) called the IntraVoxel Incoherent Motion (IVIM) method which utilises high main magnetic field strength and ultra-strong magnetic field gradients. This technology will permit completely non-invasive, quantitative characterization of tumour microvasculature at high spatial resolution over the entire breast.

Body

Hardware Development

A high strength gradient coil has been designed. The prototype coil was built with an inner diameter of 5cm, which is ideal for mice. A second coil has now been built that is more suitable for rats. This coil has an inner diameter of 24cm, which can accommodate a rat plus the equipment used to monitor the animal. The maximum gradient strength achievable with this coil is 300mT/m, which is almost ten times greater than typical clinical systems and is sufficient for the high-resolution imaging experiments proposed in this grant. Testing of the coil on both a 1.5Tesla (T) clinical MRI system and a 4T research MRI system is under way. It was found that wire density and power dissipation considerations required that the coil be constructed in a multilayer configuration. Details regarding the design and construction of the coil are given in the paper in Appendix I. This paper has been accepted by the journal MAGMA.

Pulse Sequence Development

The IVIM pulse sequence has been designed based on a standard diffusion-weighted imaging sequence. The sequence consists of a spin echo, echo planar imaging sequence with the addition of strong magnetic field gradients that cause the contrast in the images to be weighted based on the diffusion of water in the microvascular and extra-vascular compartments. We have incorporated a simple phase correction method that allows post-acquisition correction of the images for small scale motion of the object being imaged.

A computer program has been written in an interactive windows environment that allows analysis of the diffusion weighted images obtained with the IVIM pulse sequence. The program allows calculation of the diffusion coefficients either for each pixel in the images, or for the average values in a region of interest. Validation of the program has been performed using simulated data. Further validation of both the program and the IVIM sequence has been performed using phantoms that are spherical containers filled with water and acetone. The results obtained (see Appendix II) agree well with those found in the literature.

Validation of Microvascular Imaging

A tumour model has been implemented in rats using N-ethyl-N-nitrosourea (ENU). ENU is known to be a potent carcinogen that induces well vascularized mammary tumours in rats.[22] This tumour model was chosen because a range of benign and malignant tumours develop depending on the dose of ENU administered and because the tumour morphology and angiogenic behavior closely mimic breast tumours in humans. Tumours have been successfully grown in 30 rats that were given a high dose injection of ENU and in 6 rats given a low dose. IVIM images of the tumours have been obtained for each rat. High signal to noise ratios (SNR) are required in the images in order to observe the microvascular component of the measured signal. SNR's in the images have been at least 400, which should be sufficient for this study. Two of the rats were sacrificed immediately after imaging, and imaging was repeated on the sacrificed animal in order to verify that the IVIM component disappears after cessation of blood flow and is in fact due to microvascular blood flow. Preliminary results (given in Appendix III) show a fast decay component. The magnitude of the diffusion coefficient for this component is in on the order of that expected for the microvascular blood flow. This fast decay component disappears after cessation of blood flow. These results suggest that the IVIM method is capable of measuring the tumour microvasculature. Further analysis of the acquired images is underway. The tumours have been resected and pathology will be performed on each tumour to determine the degree of malignancy and the density of microvessels in the tumours. The pathological results will be correlated with the MR images.

Key Research Accomplishments

- Design of a mouse-sized gradient coil with gradient strengths that exceed 2000mT/m. (Approximately 50 to 100 times higher than typical clinical MRI systems.)
- Design of a gradient coil with an inner diameter of 24cm, which is large enough to accommodate a rat and animal monitoring equipment. Maximum gradient strengths achieved with this coil will be 300mT/m.
- Implementation of a fast MR pulse sequence that allows acquisition of diffusion weighted images with high signal to noise.
- Design and coding of a computer program that will allow automated analysis of the diffusion weighted images for the calculation of diffusion coefficients.
- Validation of the MR pulse sequence analysis program using simulated data and images acquired from substances with known diffusion coefficients.
- Implementation of a breast tumour model in rats that produces tumours with a range of malignancies from benign to malignant.
- Acquisition of *in vivo* diffusion weighted images of the tumours in the rats using the IVIM method, and preliminary analysis of the images.

Reportable Outcomes

Presentations and Publications

1. The design and construction of the gradient coils resulted in two peer-reviewed publications[23,24] and two conference presentations.[25,26] These two publications and a third publication, recently accepted by MAGMA, are appended (Appendices I, IV, and V).
2. The preliminary results of the acquisition and analysis of the images acquired from the animal tumour model were presented at the Era of Hope Meeting, Atlanta, June 8-12, 2000.

Funding

Two post-doctoral fellowships have been awarded to perform the research supported by this grant:

1. To Dr. Paula Gareau by the Department of Defense Breast Cancer Research Program of the United States Army Medical Research and Materiel Command. Grant Number BC980729.
2. To Dr. Lanette Friesen-Waldner by the Natural Sciences and Engineering Research Council of Canada.

Dr. Lanette Friesen-Waldner has recently applied for a postdoctoral traineeship to the Department of Defense U.S. Army Medical Research and Materiel Command's 2000 Breast Cancer Research Program. The research proposed in this application is based on the work supported by this award.

Conclusions

We have designed a mouse-sized gradient coil and a gradient coil large enough to accomodate rats and animal monitoring equipment. Both coils achieve gradient strengths significantly higher than typical clinical MRI systems. Based on wire density and power dissipation considerations, we have concluded that small coils with high gradient strengths, such as those required for high resolution IVIM imaging, require multilayer configurations. The design for the coils constructed here should be scalable to a breast-sized coil. Such a coil will allow imaging of the human breast at resolutions that, until now, have been unattainable, thus allowing visualisation of very small lesions within the breast.

An MR pulse sequence has been implemented on our 1.5T clinical MRI system that will allow us to acquire IVIM images with high signal to noise ratios (>400). A computer program has been written to analyse the IVIM images. The pulse sequence and analysis program have been validated using substances with known diffusion coefficients. Images have also been acquired of tumours, which were developed using an animal tumour model that we have implemented. Analysis of the images has begun and the preliminary results suggest that the tools developed here should be able to measure non-invasively the microvasculature in breast tumours. This would allow diagnosis of breast lesions *in vivo* and would also provide a means of following the effects of treatments, particularly treatment with anti-angiogenic pharmaceuticals; however, further testing of our methods is required before definitive conclusions can be drawn.

References

1. Williams SM, Kaplan PA, Petersen JC, Lieberman RP. Mammography in women under age 30: Is there clinical benefit? *Radiology* **161**:49-51, (1986).
2. Ciatto S, Cataliotti L, Distante V. Nonpalpable lesions detected with mammography: Review of 512 consecutive cases. *Radiology* **165**:99-102 (1987).
3. Dershaw DD, Shank B, Reisinger S. Mammographic findings after breast cancer treatment with local excision and definitive irradiation. *Radiology* **164**:455-461 (1987).
4. Rosen PP, Braun DW, Kinne DG. The clinical significance of breast cancer. *Cancer* **46**:919-929 (1980).
5. Folkman J. What is the evidence that tumors are angiogenesis dependent? *JNCI* **82**:4-6 (1990).
6. Sutherland RM, McCredie JA, Inch WR. Growth of multicell spheroids in tissue culture as a model of nodular carcinomas. *JNCI* **46**:113-120 (1971).
7. Folkman J, Hochberg M. Self-regulation of growth in three dimensions. *J Exp Med* **138**:745-753 (1973).
8. Sutherland RM. Cell and environment interactions in tumour microregions: The multicell spheroid model. *Science* **240**:177-184 (1988).
9. Folkman J. Angiogenesis and breast cancer. *J Clin Oncol* **12**:441-443 (1994).
10. Guidi AJ, Fischer L, Harris JR, Schnitt SJ. Microvessel density and distribution in ductal carcinoma in situr of the breast. *JNCI* **86**:614-619 (1994).
11. Bose S, Lesseer ML, Norton L, Rosen PP. Immunophenotype of intraductal carcinoma. *Arch Pathol Lab Med* **110**:81-85 (1996).
12. Chodak GW, Haudenschild C, Gittes RF, Folkman J. Angiogenic activity as a marker of neoplastic and preneoplastic lesions of the human bladder. *Ann Surg* **192**:762-771 (1980).
13. Jensen HM, Chen I, DeVault MR, Lewis AE. Angiogenesis induced by "normal" human breast tissue: A probably marker for precancer. *Science* **218**:293-295 (1982).

14. Ziche M, Gullino PM. Angiogenesis and neoplastic progression in vitro. *JNCI* **69**:483-487 (1982).

15. Folkman J, Watson K, Ingber D, Hanahan D. Induction of angiogenesis during transition from hyperplasia to neoplasia. *Nature* **339**:58-61 (1989).

16. Lawson RN. Implications of surface temperatures in the diagnosis of breast cancer. *Can Med Ass J* **75**:309-310 (1956).

17. Sterns EE, Curtis A, Miller S. Thermography in breast diagnosis. *Cancer* **50**:323-325 (1982).

18. Amalric R, Girand D, Thommasin L. The persistently abnormal isolated infrared thermogram: The highest known risk of breast cancer. *Acta Thermographia* **3**:118-124 (1982).

19. El Yousef SJ. MRI of the breast. *Radiology* **150**:761-766 (1984).

20. Heywang SH, Wolf A, Pruss E, Hilbertz T, Eiermann W, Permanetter W. MRI of the breast with Gd-DTPA: Use and limitations. *Radiology* **171**:95-103 (1989).

21. Burns PN, Halliwell M, Wells PN, Webb AJ. Ultrasonic doppler studies of the breast. *Ultrasound in Medicine and Biology* **8**:127-143 (1982).

22. Stoica G, Koestner A, Capen C. Characterization of N-ethyl-N-nitrosourea induced mammary tumors in the rat. *Am J Pathol* **110**:161-167 (1983).

23. Maier CF, Nikolov HN, Chu KC, Chronik BA, Rutt BK. Practical design of a high-strength breast gradient coil. *MRM* **39**:392-401 (1998).

24. Chronik BA, Rutt BK. Constrained length minimum inductance gradient coil design. *MRM* **39**:270-278 (1998).

25. Rutt BK, Maier CVF. Design and construction of gradient coils for diffusion breast imaging. Invited presentation at the *Society of Magnetic Resonance Breast Imaging Workshop*, Washington D.C., June 24-25, 1995.

26. Chronik BA, Alejski A, Rutt BK. A 2000mT/m multilayer gradient coil for mouse imaging. *Proceeding of the International Society for Magnetic Resonance in Medicine* 7:496 (1999).

Design and Fabrication of a Three-Axis Multilayer Gradient Coil for Magnetic Resonance Microscopy of Mice

Blaine A. Chronik, Andrew Alejski, and Brian K. Rutt

Department of Physics and Astronomy and
Department of Diagnostic Radiology and Nuclear Medicine
University of Western Ontario, and
Imaging Research Laboratories,
The John P. Robarts Research Institute,
London, Ontario, Canada N6A 5K8

Address correspondence to:

Dr. Brian K. Rutt, Ph.D.
Imaging Research Laboratories
The John P. Robarts Research Institute
P.O. Box 5015, 100 Perth Drive
London, Ontario, Canada
N6A 5K8
Phone: (519) 663-5777 x33408
Fax: (519) 663-3403
E-Mail: brutt@irus.rri.on.ca

Keywords:
Microscopy, Gradient, Coil, MRI, Multilayer, Mouse

Contents List:
Text pages:36
Figures:11
Tables:5

Abstract:

There is great interest in the non-destructive capabilities of magnetic resonance microscopy for studying murine models of both disease and normal function; however, these studies place extreme demands on the MR hardware, most notably the gradient field system. We designed, using Constrained Current Minimum Inductance methods, and fabricated a complete three-axis gradient coil set that utilizes interleaved, multilayer axes to achieve maximum gradient strengths of over 2000mT/m in rise times of less than 50μs with an inner coil diameter of 5cm. The coil was wire-wound using a rectangular wire that minimizes the deposited power for a given gradient efficiency. Water cooling was also incorporated into the coil to assist in thermal management. The duty cycle for the most extreme cases of single shot EPI is limited by the thermal response and expressions for maximum rates of image collection are given for burst and continuous modes of operation. The final coil is capable of the collection of single shot EPI images with 6mm field of view and 94μm isotropic voxels at imaging rates exceeding $50s^{-1}$.

Introduction

High speed magnetic resonance microscopy in murine models of human disease and function is of fundamental importance in a range of biomedical research areas (1,2). Non-destructive "MR histology" of brain lesions in small animals (3,4), studies of the biophysical basis of fMRI in a murine model (5), *in-vivo* diffusion-tensor microscopy (6), microscopic studies of *in utero* murine embryos (7), *in-vivo* microscopic studies of the murine carotid artery (8), and murine cardiac MRI (9,10) are all active areas of research requiring *in vivo* magnetic resonance microscopy. Cardiac MRI in the mouse heart is the most technically challenging because of the combination of small organ size (<8mm) and very fast heart rate (>450 beats per minute). The technical demands placed on the system hardware in these applications are extreme, particularly the gradient coil requirements. The small size of the mouse is of course an advantage in that it allows the use of small, customized gradient coils. This paper discusses the special considerations involved in designing such mouse-specific coils, and details the design, construction, and imaging performance of one specific design.

Above all else, very high gradient strengths are required to achieve the high spatial and temporal resolution necessary for advanced MRI of small animals. Using the fundamental relationship between gradient strength, sampling rate, and image field of view (FOV) (11), it is easily found that a 6mm FOV requires a gradient strength of 2000mT/m when using a receive signal sweep width of 500kHz, typical of the maximum sampling rate of recent generation MRI systems. This gradient strength is approximately two orders of magnitude greater than that produced by the

whole-body gradients of current clinical scanners; therefore, it is clear that a customized gradient coil is necessary for high quality mouse organ imaging.

For any given amplifier and gradient coil combination, the maximum rise time of the gradient waveforms is proportional to the coil inductance (L). For this reason, coils are often designed with minimum inductance for a given gradient strength. This minimizes the total time spent switching in any gradient waveform train, thereby minimizing TR, TE, and other critical timing parameters. The switching speed requirements for high field mouse imagers are especially extreme. For example, at 7T and above, the T2* of murine myocardial tissue is 9ms or less and the T2* of gray and white matter are 18ms and 12ms, respectively (12,13). Acquiring a 64-lobe EPI train within 20ms, using 500kHz flat-top-only sampling and a 6mm FOV, will require a minimum efficiency of 2000mT/m and a maximum inductance of 200μH. This inductance limit is up to an order of magnitude lower than that of typical clinical gradient coils.

A final and often overlooked consideration is the gradient coil duty cycle, determined by the thermal response of the coil, which is in turn largely determined by the resistance of the coil load. Because many researchers will wish to connect their mouse-sized gradient coil to a normal clinical gradient driver system, the coil must be capable of carrying high rms currents (in the range of 100A). For resistances between 0.5 and 1Ω, this corresponds to power deposition of 5 to 10kW in a physically small coil (low thermal mass) and there is the potential for a significant heating problem and a limited duty cycle. Because of the small coil size needed to achieve the strength and speed, the area available for wire cross-section is greatly reduced. In the following sections it will be demonstrated that simply scaling down existing body gradient designs is insufficient when this power deposition issue is considered. The way to achieve the required performance is to move to

multilayer coil designs while using rectangular wire to maximize copper cross-section. This method in turn creates the need to specifically consider an interleaving strategy for organizing the many layers of the coil into a complete three axis design. We outline a design strategy for interleaved multilayer, rectangular wire gradient coils in this paper, and show the experimental performance of a three-axis mouse-optimized coil created using this strategy.

Theory

Gradient Coil Scaling

As was noted in the introduction, the advantage of a customized mouse gradient coil insert is that it can be built to a small radius just large enough to encompass the mouse and RF coil assembly. We decided to design our prototype coil to an inner physical radius of 2.5cm, and therefore the innermost winding layer of the coil would have a radius of approximately 3cm. This is one order of magnitude smaller than would be typical for normal whole body gradient coils. The first question we sought to answer was what sort of performance could be expected simply by scaling a human whole-body gradient coil down to mouse size.

The four most important quantities defining the performance of a gradient coil are the efficiency (η), inductance (L), resistance (R), and temperature rise (ΔT) for a given input current. The general laws for scaling these quantities from values at radius a_o and peak winding density σ_{wo} (defined as the number of wires per cm used to wind the coil at the densest region of the wire pattern) to new radius a and density σ_w are:

$$\eta = \eta_o \cdot \left(\frac{\sigma_w}{\sigma_{wo}}\right) \cdot \left(\frac{a_o}{a}\right) \qquad [1]$$

$$L = L_o \cdot \left(\frac{\sigma_w}{\sigma_{wo}}\right)^2 \cdot \left(\frac{a}{a_o}\right)^3 \qquad [2]$$

$$R = R_o \cdot \left(\frac{\sigma_w}{\sigma_{wo}}\right) \cdot \left(\frac{a}{a_o}\right)^2 \cdot \left(\frac{A_{wo}}{A_w}\right) \qquad [3]$$

where A_w is the cross-sectional area of the wire. Resistance is of importance in this application because of its influence on the thermal response of the coil. The average temperature increase of a coil is proportional to resistance and inversely proportional to the total volume of the coil wall (assuming that the material properties remain constant with temperature). Assuming that the volume scales as the cube of the radius and that A_w scales inversely with the square of the winding density (as they would for uniformly scaled coil and wire dimensions), then the temperature change at any constant rms current is expected to scale as:

$$\Delta T = \Delta T_o \cdot \left(\frac{\sigma_w}{\sigma_{wo}}\right)^3 \cdot \left(\frac{a_o}{a}\right). \qquad [4]$$

Figure 1 contains plots of η, L, and ΔT as a function of radius for several fixed values of winding density. The starting point used to generate these plots was a hypothetical "typical" body-sized gradient coil design with a radius of 30cm, efficiency of 0.12mT/m/A, inductance of 1200μH, resistance of 500mΩ, temperature change of 5°C at an rms current of 100A, and a maximum winding density of $2cm^{-1}$.

For a clinical amplifier system capable of delivering a peak current of 200A, the gradient efficiency required to achieve 2000mT/m is 10mT/m/A. Examining figure 1a we note that a winding density of $16cm^{-1}$ or higher is required to achieve 10mT/m/A for a radius of 3cm. This is itself a limitation in that constructing such a dense wire pattern is quite difficult with standard methods;

furthermore, the wire would have to be of such small cross section as to preclude the high peak currents (on the order of the 200A) required. Construction methods developed in our lab currently produce a maximum wire density of approximately $8cm^{-1}$ on a single transverse layer, but according to the efficiency plot this only produces approximately half of the required strength. One way to reach higher effective density wire patterns with lower density fabrication methods is to divide the winding of a single layer across two or more layers, each individual layer wound at the highest density achievable.

The inductance variation depicted in figure 1b indicates that coils at the highest σ_w values considered fall below the 200μH upper limit allowed for this application. The figure indicates that a single layer design wound at $8cm^{-1}$ would have an inductance of 20μH at a 3cm radius. To a first approximation, the inductance of a double layer $8cm^{-1}$ coil operated in series is equivalent to that of an equal radius single layer design wound to $16cm^{-1}$, i.e. 80μH at a 3cm radius; therefore, it is expected that the two layer configurations needed to achieve the efficiencies discussed in the previous paragraph will also result in inductance values below the specified upper limit.

The thermal response of small, high winding density coils represents the dominant practical limitation, as is evident from figure 1c. Scaled to the desired mouse coil radius, all winding densities result in steady-state coil temperatures orders of magnitude higher than would be tolerable. For this reason, we expect that all mouse coils meeting the specifications outlined will have extreme duty cycle limitations unless special effort is made to minimize the temperature increases. We argue in this paper that this consideration leads to a dominant requirement for minimum resistance configurations, which requires the combination of rectangular cross-section wire

with multilayer designs in order to achieve the smallest resistance for a given effective winding density.

Heating

The temperature response of a gradient coil when driven by an rms current (I_{rms}) can be approximated by an exponential approach to an equilibrium temperature (14) and the following equation relating temperature (T) and time (t) applies to both heating and cooling of the coil:

$$T = T_o + \Delta T_{ss} \cdot \left[1 - \exp\left(\frac{-t}{\tau}\right)\right] \qquad [5]$$

where ΔT_{ss} is the steady state temperature change at the measurement location, T_o is the temperature at the start of the measurement, and τ is a time constant characteristic of the axis and the degree of cooling applied. For the heating phase, a steady-state heating parameter can be defined:

$$k_h = \frac{\Delta T_{ss}}{I_{rms}^2 R} \qquad [6]$$

where I_{rms} is the rms current applied and R is the resistance of the axis. To a first approximation, ΔT_{ss} is simply proportional to the input power while τ is independent of it (14); therefore, assuming that resistance is constant over the range of temperatures in the experiment, k_h is a constant for each axis and rate of water cooling and it can be used to calculate the steady-state temperature increase for any input power.

The fact that τ is independent of the input power means that it is an operationally independent parameter that can be used to define the transition between two modes of coil operation. These two modes require individual consideration when calculating duty cycles. To achieve scan repeti-

tion (TR) times much less than τ, the coil may be operated in a burst mode, during which it is run at high power for a short time (t_b, the burst time) and allowed to heat-up at an unsustainable rate (figure 2a). This would then have to be followed by a dead time, t_d, during which the coil is allowed to cool sufficiently before starting another burst phase. This operation mode would be required when imaging at very high rates is important but required only for short blocks of time; an example might be cardiac imaging. For this mode, the maximum number of single shot EPI images that can be collected during each burst phase was calculated as a function of the pulse sequence and coil thermal parameters such that the coil temperature increases were maintained at tolerable levels.

For scan times on the order of τ and longer, the coil must be run in a sustainable fashion, and the steady-state thermal response is of primary importance. In this continuous mode (figure 2b), the minimum TR for repeated single shot EPI imaging was calculated as a function of the pulse sequence parameters such that the corresponding rms current resulted in a tolerable steady-state temperature increase. Burst and continuous mode operation are analyzed in more detail in the following paragraphs.

The purpose of burst mode operation is to allow images to be collected at the minimum sequence repetition time defined by timing rather than by heating considerations. The length of time that this can be sustained (t_b) is determined by the rms current applied during the burst (I_{rms_b}), the temperature excursion allowed to develop during the burst (ΔT_b), and the heating parameters of the coil. Ignoring the heating contributions from the phase encode and slice select axes, the rms current that exists during each single shot EPI collection can be approximated as:

$$I_{rms\_b} \cong \left(\frac{2\pi \cdot SW}{\gamma \eta_r FOV_r}\right) \cdot \sqrt{\frac{N_p}{TR}} \cdot \left\{\frac{2}{3} \cdot \frac{L_r}{V} \cdot \frac{2\pi \cdot SW}{\gamma \eta_r FOV_r} + \frac{N_r}{SW}\right\}^{1/2} \quad [7]$$

where: SW is the receive signal sweep width, γ is the gyromagnetic ratio of the nucleus, η_r is the gradient efficiency of the readout axis, FOV_r is the field of view in the direction of the readout axis, N_p is the number of phase encode lines, TR is the time between EPI collections, L_r is the inductance of the readout axis, V is the voltage applied during gradient slewing, and N_r is the number of readout points collected. Applied for an infinite amount of time, this rms current would typically result in an extremely high steady state temperature increase found by solving equation [6] for the temperature:

$$\Delta T_{ss\_b} = k_h \cdot I_{rms\_b}^2 \cdot R. \quad [8]$$

This steady state temperature increase is used within equation [5] to obtain the coil temperature as a function of time. For burst mode operation, the initial slope of the temperature response is critical and the temperature curve can be approximated for $t_b << \tau$ to give:

$$\Delta T_b = \frac{\Delta T_{ss\_b}}{\tau} \cdot t_b \quad [9]$$

where the temperature increase at any given instant is defined as $\Delta T_b = T - T_o$. The maximum number of images (N_{burst}) that can be collected within a single burst is simply the burst time divided by the minimum sequence TR. Solving for t_b via equations [9] and [10] and dividing by TR we obtain:

$$N_{burst} = \frac{\Delta T_b}{(I_{rms\_b})^2 R} \cdot \frac{\tau}{k_h} \cdot TR^{-1}. \qquad [10]$$

Equations [7] and [10] yield the following general expression for the maximum number of images that may be collected as a function of the pulse sequence parameters, the maximum tolerable ΔT_b, and the readout axis heating parameters (k_h and τ):

$$N_{burst} = \frac{\Delta T_b}{N_p} \cdot \frac{\tau}{k_h R} \cdot \left(\frac{\gamma \eta_r FOV_r}{2\pi \cdot SW}\right)^2 \cdot \left[\frac{2}{3} \cdot \frac{L_r}{V} \cdot \frac{2\pi \cdot SW}{\gamma \eta_r FOV_r} + \frac{N_r}{SW}\right]^{-1} \qquad [11]$$

Using this expression, N_{burst} was computed as a function of the FOV for different imaging parameters and choice of gradient axis used for readout. Note that TR has factored out of the expression. Although shorter TRs allow for faster imaging, they also result in shorter allowable t_b; therefore, the two effects cancel each other and the number of images allowed stays constant. The last piece of data that is necessary to characterize burst mode operation is the length of dead time (t_d) required between bursts. One simple specification is to require that the rms current calculated over an entire cycle ($t_b + t_d$) lead to an rms temperature increase (ΔT_{rms}) over baseline equal to ΔT_b, the burst time temperature increase (see Figure 2a). In this case, the following simple relationship between t_b, t_d, and τ can be shown to hold:

$$t_b + t_d = \tau. \qquad [12]$$

Equation [13] indicates that imaging can only be done for a period of t_b once every heating time constant of the readout axis. The long-term average rate of image collection (i.e. averaged over many burst cycles) is independent of τ because although a smaller τ allows fewer images to be

collected per burst (equation [11]), it also allows more burst periods per unit time (equation [13]) and the two effects cancel.

Continuous mode operation is simply governed by adjusting the single shot EPI image repetition time, TR, such that the coil can be sustainably operated. A tolerable steady state temperature excursion, ΔT_c, must be chosen (figure 2b), and equation [6] is used to calculate the corresponding I_{rms} current. Equation [7] is solved for TR and combined with equation [6] to yield:

$$TR_{min} = N_p \cdot \left(\frac{k_h}{\Delta T_c}\right) \cdot \left(\frac{2\pi \cdot SW}{\gamma \eta_r FOV_r}\right)^2 \cdot \left\{\frac{2}{3} \cdot \frac{L_r}{V} \cdot \frac{2\pi \cdot SW}{\gamma \eta_r FOV_r} + \frac{N_r}{SW}\right\}. \qquad [13]$$

Using this expression, minimum TR was computed as a function of the FOV for different imaging parameters and choice of gradient axis used for readout.

Methods

Optimized Layer Design

With the need for multilayer, rectangular wire designs identified, there remains the issue of finding the best design for the individual layers. The three axes of a gradient coil set can be broken into two design groups: the transverse (X and Y) and the longitudinal (Z) axes. The X and Y axes use the same design, one obtained from the other via a ninety degree rotation about the longitudinal axis. The strategy for selecting the optimal design is the same for both transverse and longitudinal coils and we will focus on the former.

All designs were obtained using the method of Constrained Current Minimum Inductance (CCMI) reported previously (15). Specifically, the CCMI method is a solution for the minimum

inductance current density satisfying a set of field constraints, and subject to a set of constraints on the current density itself. The current constraints define the region over which the current is allowed to flow and therefore specify the design's aspect ratio, defined as the ratio of the coil's total length to its diameter. The field constraints are placed in such a way as to define the region of uniformity (ROU). By varying both the arrangement of the field constraints and the limits of the current constraints, designs can be obtained for any combination of ROU and aspect ratio, and for each design the gradient efficiency, inductance and winding density can be calculated. The simplicity and computational efficiency of the CCMI method offer the unique opportunity to directly model all possible designs in the ROU, aspect ratio parameter space. By plotting design performance figures over this space at the winding density and radius of the desired coil, the entire range of achievable performance is made apparent while trade-offs between imaging region size and coil size can be rapidly visualized and understood. The choice of the optimal design then becomes a straightforward matter of locating the best coordinate in this space for the given application.

An additional complexity in our application was the requirement for a small side aperture (1cm in diameter) for lateral sample/probe access. This feature required the application of current constraints (via CCMI) about the z centre of the design and the effects of this process will be described in more detail elsewhere.

Interleaving

In the theory section it was noted that a multilayer configuration would be needed in this application to achieve the required gradient strengths. It was also suggested that rectangular wire would be of significant benefit in minimizing the resistance for any winding density, and therefore

maintaining tolerable thermal response for the coil. The complicating issue in small radius, multilayer coils with rectangular wire is that the thickness of each winding layer becomes a significant fraction of the radius. This is not a major concern when only one axis of a gradient coil is being built; however, it becomes a problem when all axes of the coil are being considered together. In most imaging applications it is not often useful to have one axis significantly stronger than the others. If a multilayer coil is simply wound consecutively from the first axis to the last as in figure 3a, the width of the layers will force the effective radius of the outermost axis to be significantly larger than the innermost, resulting in an appreciable performance imbalance. The alternate approach is to interleave the layering order in such a way as to equalize the strength, an example of which is shown in figure 3b. The interleaving question becomes that of determining the effects of different distributions of the layers of the three axes into the allowed radial positions.

In preliminary fabrication tests for this design, it was determined that an entire single layer, including return paths and potting considerations, could be achieved with a wall thickness of 7mm. With the radius of the inner bore set at 2.5cm and assuming a five layer construction (the choice of a five layer construction is explained in the results section), the outer radius of the coil would be 6.0cm. The effective wire pattern radius for each layer was chosen to be 2.75mm larger than the inner radius of that layer, yielding radii of 2.775cm, 3.475cm, 4.175cm, 4.875cm, and 5.575cm for layers one through five, respectively. There are fifteen distinct possibilities for distributing the three axes over the five layers and they were each modeled by scaling the chosen transverse and longitudinal coil designs to the above radii. The winding density was set to $8cm^{-1}$ for each of the transverse layers and to $10cm^{-1}$ for the longitudinal layer. The two layers of each

transverse axis were modeled as a series connection. The field gradients and inductances were calculated from the resulting wire patterns using the Biot-Savart law and Neumann formula, respectively (16).

Fabrication

The fabrication process was developed and carried out completely within our labs over a three month period. Predominantly carried out by a single individual, the estimated total cost of the project was $20,000 dollars (CAD). The general procedure has been developed during the construction of several previous gradient coils and was customized as required for this project. Of special concern was the production of a very robust gradient coil capable of operation at high currents within a typical clinical scanner. For this reason special attention was paid to the potting procedures as described below.

The wire used was composed of 119 strands of 36 AWG copper wire arranged in a Litz braiding to produce a rectangular cross section wire 0.8 x 3.5 mm^2 in size with an equivalent gauge of 16 AWG (New England Electric Wire Corporation, New England, USA). Individual conducting elements were coated with insulation heat rated to 150° C. Litz wire was used in place of solid copper to reduce resistance at frequencies of several kHz, expected to be the dominant operating frequency of the coil for high speed imaging sequences. The DC resistance of the wire was 13mΩ/m. The multistrand formation of the Litz wire also improved its workability, reducing wire

memory and allowing a minimum bending radii of several mm. In comparison, winding the transverse axis patterns with equal area solid copper wire was found to be exceedingly difficult.

The wire patterns for each layer were CNC milled into the outer surfaces of teflon cylinders using a 3-axis cylindrical mill developed and constructed within our labs for the specific purpose of gradient coil fabrication. A complete pattern for a single transverse layer could be cut in approximately 6 hours in a single pass. Grooves were milled 1.75mm deep (half the height of the wire) and precisely 0.8mm wide such that when the wire was pushed into the grooves, it would be held in the plastic former while extending 1.75mm out of the cylinder wall.

The winding of the layers proceeded relatively slowly, typically taking a single person an average of 18 hours to finalize each layer. After winding each layer, a light coating of epoxy was applied to help hold the wire in place and to fix a type-E thermocouple over the wire at the location of maximum wire density. These thermocouples allow active temperature monitoring of the hottest areas of the coil, thereby permitting thermal characterization of the coil as discussed below, as well as the continual monitoring of the coil during operation to prevent accidental damage. The pattern for each layer was wound with one continuous length of wire to avoid the presence of solder connections within the wall of the coil, the most probable site for thermal failure in our experience. The five wound layers were then potted together into one single cylinder. A 1.5 cm thick layer containing 7mm diameter copper tubing carrying forced water cooling at flow rates of up to 5l/min was potted around the exterior of the coil to form the outermost layer. The epoxy used for the potting (Durapot 865, Cotronics Corporation, New York, USA) was specially chosen to have a very high thermal conductivity (2.8W/m/K) so that the cylinder wall could effectively transfer heat from the wire layers to the outer cooling tubes. The epoxy was heated before potting

to reduce its viscosity and the entire coil structure was mechanically agitated during the first few hours of curing to assist the penetration of epoxy and prevent air pocket formation. The potting was accomplished in stages, one for each layer, with each stage requiring a minimum of 24 hours to allow the epoxy to cure.

The aperture designed for the side of the coil was maintained during the potting procedure and then honed as a final step to assure an aperture clear bore diameter of 1cm. Figure 4 shows a photograph of the completed coil before the addition of the outermost cooling layer. Connections between layers were made via heavy-duty copper jumpers at the back of the coil. Thermocouple lead connectors were potted into the back wall of the coil for stability. The inner diameter is 5cm, outer diameter is 15cm, and total coil length (including cable connection posts and cooling connectors) is 25cm. The completed coil weighs approximately 23lbs.

Heating

Using thermocouples incorporated into the coil during construction, internal temperature measurements were made over time while passing 20A DC through each axis in turn. Heating was halted when internal coil temperatures increased by 30°C. The cooling rate of the coil was measured by recording the internal temperature as a function of time after the cessation of current. The experiment was repeated for each axis for water flow rates of 0l/min and 4l/min. Both ΔT_{ss} and τ were obtained by applying a least-squares fit to the experimental curves for each axis (equation [5]), during both heating and cooling phases.

Electrical Measurements and Imaging

Bench top measurements of both resistance and inductance were made at frequencies of 1kHz and 10kHz using a Hewlett-Packard 4262A LCR meter.

The completed coil was directly interfaced with both a Varian-Siemens Unity INOVA 4T whole body scanner (peak current: 250A, peak voltage: 600V) and a 1.5T General Electric Signa Horizon with Echospeed gradient amplifiers (peak current: 200A, peak voltage: 1200V, General Electric Medical Systems, Milwaukee, WI). No eddy current compensation was applied for any of the sequences run. The coil was well fixated within the magnet bore in each circumstance. Individual solenoidal RF coils (18mm and 34mm in diameter) were constructed and tuned to resonate within the gradient coil bore for both field strengths.

The gradient efficiency was measured by imaging a precision grid phantom (square in plane grid elements of size 2 x 2 mm^2) using a known current. After reconstruction, the image measurements were used in conjunction with the known phantom dimensions to adjust the gradient efficiency until the grid elements in the centre of the image were of the correct dimension.

Results

Optimized Layer Design and Interleaving

Figure 5 shows a contour plot of η in mT/m/A over the parameter axes of ROU and coil length for a fixed winding density of $8cm^{-1}$ and radius of 2.775cm. The ROU for the purposes of this plot is taken to be the longitudinal length of the region within which the absolute value of the gradient inhomogeneity is less than 30%; however, the relative features of the plot are unchanged with the use of more stringent homogeneity specifications defining the ROU. For aspect ratios

below approximately 1.5 (coil length of approximately 8cm on the plot), the general trend is that the most efficient designs correspond to the regions of smallest ROU and longest coil; however, the trend for aspect ratios above about 1.6 (coil length of approximately 9cm on the plot) is that the designs get more efficient as both the coil length and ROU are increased. The dependency of η on coil length (aspect ratio) is essentially monotonic over the entire plot with increasing length resulting in more efficient designs.

For mouse imaging with minimal gradient distortion over the heart region (<1cm in diameter (10)) and correctable distortion over a region large enough to image the mouse body if desired (~3cm in diameter (10)) a region of better than 1% homogeneity was required over 1cm and 30% over 3cm diameter spherical volumes (DSV). Taking the 30% DSV as the primary homogeneity constraint, a line can be drawn on the design space contour plot (figure 5) to indicate the region of coils that can be considered. If there were length constraints for this coil, a horizontal line at that maximum length could also be added to further limit the region under consideration. In this application there is no such constraint and the entire plot to the right of the DSV line is allowed. The chosen design is at the point defined by a coil length of 11.1cm and an ROU size of 3.3cm (indicated by a star on figure 5). The higher efficiency region above and to the right of the selected design was excluded because of increased inductance values associated with that area of the space. The optimal layer design for the longitudinal axis was obtained in the same manner. The calculated values of σ_w, η, L, and R are listed in the first row of table 1 for the innermost winding radius of 2.775cm. All other layers of both the X and Y axes were based on the design of figure 6a, each scaled to the appropriate radius while maintaining an approximately constant winding density of $8cm^{-1}$. The calculated performance values for each of these layers are also shown in

table 1. The wire patterns for a single octant of the transverse and longitudinal layers are shown in figures 6a and 6b respectively. The layer ordering implicit in table 1 is the optimal one as determined from the interleaving results described below.

Table 2 lists the calculated results for the possible layer orderings. The most unbalanced case (XXZYY) results in a range of efficiency of 74% (X largest, Y smallest) and a range of inductance of 332% (Y largest, X smallest). For the most balanced ordering (XYZYX), the efficiency and inductance ranges were reduced to 14% and 25%, respectively. In this application it was decided that the most balanced combination was best and therefore the XYZYX interleave was used.

We also investigated the benefit of adding additional layers to the designs. All possibilities were modeled, and the results summarized in table 3. Looking at the most efficiency balanced example (XYZYXYXZ), it is seen that the average efficiency of the transverse axes increases by 29% while the average inductance increases by 242%. This may be warranted in situations where switching speed is not important or where the larger inductance is needed to simplify interfacing the coil with existing amplifiers; however, in this application it was decided that the increases were not useful.

Electrical Performance

The measured values for resistance and inductance of the individual layers as well as the complete axes are summarized in table 4. The calculated values are also included for comparison. It should be noted that the relatively slow increase of resistance with frequency is expected because of the Litz wire construction. The calculated resistance values are generally lower than the experimental results because they assume zero frequency (DC) and they do not take into account the

length of connecting wire within the coil or the effects of linking the wire to the brass connection posts. These effects are negligible for inductance, as indicated by the accuracy of the inductance calculations as compared to the measurements.

Heating

The results of temperature measurements as a function of time for the x axis during periods of heating and subsequent cooling are shown in figure 7. Superimposed on the data points are the best-fit curves based on equation [5]. The heating curves for both the y and z axes are similar. The fitted values of ΔT_{ss} and τ for all measurements are summarized in table 5. Table 5 also includes the corresponding values of k_h as defined in equation [6]. The data indicates that the steady state heating parameter, k_h, is decreased by an average of 46% with the addition of water cooling (46%, 21% and 70% for the X,Y, and Z axes, respectively). The heating time constant (τ_h) is always found to decrease with cooling, whereas the cooling time constant (τ_c) always increases (although only very slightly for the z axis). The most important effect of cooling is evident by noting the difference in steady state temperature decreases. These results suggest that without cooling the steady state temperatures of the coil, after the cessation of power, approach on average approximately 15°C above ambient temperature. Of course, eventually the coil would cool to room temperature; however, this full return to baseline temperatures required several hours. In practice, this would represent a serious limitation to coil performance. The addition of cooling removed this limitation and resulted in cooling times very close to heating times (noted by the similarity between τ_h and τ_c with the inclusion of cooling).

Figure 8 shows the number of single shot EPI images that can be collected at maximum rate (as determined by the pulse sequence) during each burst period as a function of FOV for each

axis. The x axis allows the collection of the largest number of images before each dead time (14% more than the z axis, 57% more than the y axis); however, this is balanced by the fact that the entire burst plus dead time sequence can be repeated every 430 seconds when using the z axis, as compared to 631 and 666 seconds for the Y and X axes, respectively. In practice, burst mode cannot be accomplished repeatedly without water cooling because of the extremely long times required for the coil to cool.

Figure 9 shows a plot of the minimum single shot EPI repetition time as a function of the read-out FOV for the three individual axes. The z axis allows an imaging rate approximately two times that of y and 50% more than x over the full range of FOVs, while the x axis demonstrates an approximate 30% speed advantage compared to the y. A similar analysis can be used to compare the performance of each axis with and without water cooling and it was found that the z axis showed a decrease in minimum TR by 70%, the x axis by 45%, and the y axis by 20% with the use of water cooling.

Preliminary Imaging

Figure 10 shows the first image collected, on the 4T scanner, of the grid phantom as described in the Methods section. It was collected with a gradient-recalled echo sequence with the following parameters: TR = 50ms, TE = 4ms, flip angle = 11°, matrix size = 256 x 256, FOV = 4 x 4 cm^2, slice thickness = 2mm, and number of averages = 16. The image in the figure is cropped to highlight the grid phantom of size 26mm square. A box has been overlaid on the image to indicate a region of 1cm square that corresponds to the size of the ROU over which less than 1% deviation was expected. It can be seen that no obvious image distortions occur over that area. The

measured efficiencies at the coil center for the X, Y, and Z axes were found to be 11.8 mT/m/A, 11.0 mT/m/A, and 11.2 mT/m/A respectively.

Figure 11 shows a proton-density-weighted fast spin-echo image of an excised rat brain collected on a GE 1.5T Signa scanner. The sequence parameters were: TR = 3500ms, effective TE = 18ms, matrix size = 256 x 192, FOV = 1.7 x 1.7 cm^2, slice thickness = 0.625mm, echo train length = 4, and number of averages = 24. Total imaging time was approximately one hour and fifteen minutes. The in-plane resolution was 65 x 87 μm^2. The smooth, round outer surface of the brain is due to the 14mm diameter tube into which the brain was placed during imaging.

Discussion

Although there are numerous publications describing gradient coil designs (17), descriptions of coils customized for small animal imaging are lacking. A body of work does exist for the development of very small, extremely high strength designs for use in NMR diffusion studies in very small (typically less than $1cm^3$) samples (18-28). The very small coils described for these studies are typically one or two axis designs and hence are not suitable for microimaging studies (22-24). Quadrupolar designs (for at most two axes) are the most popular in these applications (19, 20, 23-25, 29, 33, 34), assuming that there is adequate room within the scanner bore for transverse coil alignment. Coils in the transverse orientation (29, 33-35) and on-axis (30-32,36) have been reported that are large enough be used for small animal studies while multilayer designs for single axes have been reported (26-28) for diffusion NMR studies, but there are no complete three axis designs considered that apply multilayer design methods, nor have multilayer methods been applied to the design of coils large enough for small animal imaging. A survey of the literature

indicates that the strongest on-axis gradient coils in use for mouse imaging produce gradients of up to 1000mT/m (10). The trade-offs between coil aspect ratio, imaging ROU, and coil performance have not been demonstrated previously, nor have the special considerations that must be taken into account to properly govern coil heating.

This paper demonstrates that the primary challenges to attaining the extreme gradient strength and speed requirements that accompany mouse imaging pertain to the thermal response of the coil. To alleviate the extreme heating problems predicted by the thermal scaling laws described in the theory section, efforts were made on several fronts to manage the temperature of the coil while maintaining the required strength and inductance. A multilayer approach was taken that allowed high efficiency designs with reduced winding density. The lower winding densities are vital in that they allow larger cross-section wire to be used, thereby reducing resistance significantly. We developed fabrication methods that allow the use of rectangular Litz wire. The rectangular wire was wound on end, increasing the available copper area by a factor of four (for the particular wire used in this coil) as compared to square wire wound to the same density. The Litz wire was chosen for its resistance characteristics over the 1 to 10 kHz range, expected to be the dominant operating frequency for the high speed image acquisitions intended for this coil. These measures all contributed to reducing the resistance of each axis. Going further, we sought to reduce the temperature increases for any input power through the addition of water cooling. The epoxy used for the fabrication of the coil was specially chosen to have the highest thermal conductivity available. This maximized the transfer of heat from the wires to the water cooling layer. The potting procedure was specially developed to avoid the inclusion of any heat insulating materials that would hinder the removal of heat from the coil. Thermocouples were built into the coil to allow both the

characterization of the heating response of the coil under various circumstances, as well as to facilitate continual thermal monitoring during operation. Finally, efforts were made to model the heating effects of two very different modes of operation. These efforts all contributed to attaining optimal performance with the final coil.

It is instructive to compare the thermal response as predicted by the initial scaling laws to the measured response of the completed coil. From figure 1, we saw that if the hypothetical body coil were simply scaled down to mouse size, a winding density of $16cm^{-1}$ would have been required to achieve the target efficiency. The corresponding steady-state temperature increase at 100A was seen to be approximately twenty-five thousand degrees, clearly not feasible and underlining the need for a different approach. From the heating measurements made and summarized in table 5, we saw that for an input rms current of 20A, the average steady-state temperature increase of the axes was 32°C. Scaling this result to an input rms current of 100A, the temperature increase of the axes is predicted to be approximately 800°C. Although still a much larger temperature increase than tolerable, it is more than thirty times lower than that predicted by the uniform scaling law. This substantial improvement is due to the many steps taken to limit the heating of this mouse coil.

The results indicate that this coil design can be successfully operated in both burst and continuous modes. In different applications, both will be necessary and it is important to be able to optimize the coil duty cycle for either case. Burst mode will allow the collection of hundreds of successive <1cm FOV single shot 64 x 64 EPI images at rates of approximately 60 images per second. Continuous mode will allow steady collection of <1cm FOV single shot 64 x 64 EPI images at rates of approximately one per second. These are of course the extreme cases with

respect to FOV. Practical operation will undoubtably involve some compromise between FOV and imaging rates; the theory and results described in this paper can be applied to optimize the coil operation in any circumstance.

There are several ways that the coil design presented here can be improved. Firstly, minimum power instead of minimum inductance methods could have been applied and this may have reduced the axis resistance at the cost of increased inductance (17). The reason that this was not done was that we have not implemented minimum power methods in conjunction with current constraints, as we have with CCMI. The use of current constraints is important to control the final size of the coil and was necessary to achieve the side-hole aperture specified. Secondly, more elegant minimum power 3D methods for multilayer gradient coils have been reported recently (26,28). It would be possible to utilize those techniques to obtain an equivalent strength coil with lower resistance in place of simply scaling the size of a single design to the different layers. Again, this is expected to be at the cost of increased inductance. We focused primarily on improved fabrication methods to minimize the thermal problems in this coil; however, because temperature response remains the dominant limiting factor in this coil, additional design optimization efforts are warranted.

Conclusion

This paper has demonstrated the most important issues in the design and operation of a very high strength gradient coil for small animal microscopy. With current generation amplifier hardware, this coil allows the collection of single shot EPI images at 6mm FOV and 94μm isotropic

voxels at imaging rates exceeding $50s^{-1}$. This coil should allow improvements in *in vivo* MR microscopy for a diverse range of applications.

Acknowledgments

The authors would like to thank Carl Gazdzinski for his work in analyzing the designs required to visualize the coil parameter space. We also thank Dr. Greg Stanisz for his assistance with the heating measurements and Dr. R. M. Henkelman for his valuable suggestions. BAC was supported by a Natural Sciences and Engineering Research Council of Canada postgraduate scholarship. This work was supported in part by the Medical Research Council of Canada grant GR-14973.

References

[1] Chien KR. Genes and Physiology: Molecular Physiology in Genetically Engineered Animals. J Clin Invest 1996; 97:901-909.

[2] Johnson GA, Benveniste H, Engelhardt RT, Qiu H, Hedlund LW. Magnetic Resonance Microscopy in Basic Studies of Brain Structure and Function. Annals New York Acad Sciences 1997; 820:139-148.

[3] Lester DS, Lyon RC, McGregor GN, Engelhardt RT, Schmued LC, Johnson GA, Johannessen JN. 3-Dimensional Visualization of Lesions in Rat Brain Using Magnetic Resonance Imaging Microscopy. NeuroReport 1999; 10:737-741.

[4] Kooy RF, Reyniers E, Verhoye M, Sijbers J, Bakker CE, Oostra BA, Willems PJ, Van Der Linden A. Neuroanatomy of the Fragile X Knockout Mouse Brain Studied Using High Resolution Magnetic Resonance Imaging. Eur J Hum Genet 1999; 7:526-532.

[5] Grune M, Pillekamp F, Schwindt W, Hoehn M. Gradient Echo Time Dependence and Quantitative Parameter Maps for Somatosensory Activation in Rats at 7T. Magn. Reson. Med. 1999; 42:118-126.

[6] Fenyes DA, Narayana PA. In Vivo Diffusion Tensor Imaging of Rat Spinal Cord With Echo Planar Imaging. Magn. Reson. Med. 1999; 42:300-306.

[7] Smith BR, Shattuck MD, Hedlund LW, Johnson GA. Time-Course Imaging of Rat Embryos In Utero with Magnetic Resonance Microscopy. Magn Reson Med 1998; 39:673-677.

[8] Arnder L, Zhou X, Cofer G, Hedlund LW, Johnson GA. Magnetic Resonance Microscopy of the Rat Carotid Artery at 300 Megahertz. Invest Radiol 1994; 29:822-826.

[9] Rose SE, Wilson SJ, Zelaya FO, Crozier S, Doddrell DM. High Resolution High Field Rodent Cardiac Imaging With Flow Enhancement Suppression. Magn Reson Imag 1994; 12:1183-1190.

[10] Slawson SE, Roman BB, Williams DS, Koretsky AP. Cardiac MRI of the Normal and Hypertrophied Mouse Heart. Magn Reson Med 1998; 39:980-987.

[11] Callaghan PT. Principles of Nuclear Magnetic Resonance Microscopy. New York: Oxford University Press; 1991.

[12] Cremillieux Y, Ding S, Dunn JF. High-Resolution In Vivo Measurements of Transverse Relaxation Times in Rats at 7 Tesla. Magn Reson Med 1998; 39:285-290.

[13] Meyerand ME, Cremillieux Y, Wadghiri YZ, Azzawi A, Hoopes PJ, Dunn JF. In Vivo Gradient Echo Microimaging of Rodent Spinal Cord at 7T. Magn Reson Med 1998; 40:789-791.

[14] Chu KC, Rutt BK. MR Gradient Coil Heat Dissipation. Magn Reson Med 1995; 34:125-132.

[15] Chronik BA, Rutt BK. Constrained Length Minimum Inductance Gradient Coil Design. Magn Reson Med 1998; 39:270-278.

[16] Reitz JR, Milford FJ, Christy RW. Foundations of Electromagnetic Theory, 4th ed. New York: Addison-Wesley; 1989.

[17] Turner R. Gradient Coil Design: A Review of Methods. Magn Reson Imag 1993; 11:902-920.

[18] Parker RS, Zupancic I, Pirs J. Coil System to Produce Orthogonal, Linear Magnetic Field Gradients. J Phys E: Sci Instrum 1973; 6:899-900.

[19] Webster DS, Marsden KH. Improved Apparatus for the NMR Measurement of Self-Diffusion Coefficients Using Pulsed Field Gradients. Rev Sci Instrum 1974; 45:1232-34.

[20] Odberg G, Odberg L. On the Use of a Quadrupole Coil for NMR Spin-Echo Diffusion Studies. J Magn Reson 1974; 16:342-347.

[21] Zupancic I, Pirs J. Coils Producing a Magnetic Field Gradient for Diffusion Measurements With NMR. J Phys E: Sci Instrum 1976; 9:79-80.

[22] Cho ZH, Ahn CB, Juh SC, Lee HK, Jacobs RE, Lee S, Yi JH, Jo JM. Nuclear Magnetic Resonance Microscopy with 4-μm Resolution: Theoretical Study and Experimental Results. Med. Phys. 1988; 15:815-824.

[23] Schoeniger JS, Blackband SJ. The Design and Construction of a NMR Microscopy Probe. J Magn Reson B 1994; 104:127-134.

[24] Rofe CJ, Van Noort J, Back PJ, Callaghan PT. NMR Microscopy Using Large, Pulsed Magnetic Field Gradients. J Magn Reson B 1995; 108:125-136.

[25] Oishi O, Miyajima S. New PFG NMR Spectrometer with a Rotatable Quadrupole Coil for the Measurement of an Anisotropic Self-Diffusion Coefficient Tensor. J Magn Reson A 1996; 123:64-71.

[26] Bowtell R, Robyr P. Multilayer Gradient Coil Design. J Magn Reson 1998; 131:286-94.

[27] Snaar JE, Robyr P, Bowtell R. Strong gradients for spatially resolved diffusion measurements. Magn. Reson. Imag. 1998; 16:587-91.

[28] Bowtell R, Crozier S, Beck B, Blackband S. Multi-Layer Transverse Gradient Coils. In: Proceedings of the ISMRM, 1999. p468.

[29] Bowtell R, Mansfield P. Screened Coil Designs for NMR Imaging in Magnets with Transverse Field Geometry. Meas. Sci. Tech. 1990; 1:431-439.

[30] Wong EC, Jesmanowicz AJ, Hyde JS. High-Resolution, Short Echo Time MR Imaging of the Fingers and Wrist with a Local Gradient Coil. Radiol 1991; 181:393-397.

[31] Eccles CD, Crozier S, Roffman W, Doddrell DM, Back P, Callaghan PT. Practical Aspects of Shielded Gradient Coil Design for Localised In Vivo NMR Spectroscopy and Small-Scale Imaging. Magn Reson Imag 1994; 12:621-630.

[32] Blackband SJ, Chakrabarti I, Gibbs P, Buckley DL, Horsman A. Fingers: Three-Dimensional MR Imaging and Angiography with a Local Gradient Coil. Radiol 1994; 190:895-899.

[33] Chu KC, Rutt BK. Quadrupole Gradient Coil Design and Optimization: A Printed Circuit Board Approach. Magn. Reson. Med. 1994; 31:652-659.

[34] O'Dell WG, Schoeniger JS, Blackband SJ, McVeigh ER. A Modified Quadrupole Gradient Set for Use in High Resolution MRI Tagging. Magn Reson Med 1994; 32:246-250.

[35] Maier CF, Chu KC, Chronik BA, Rutt BK. A Novel Transverse Gradient Coil Design for High-Resolution MR Imaging. Magn. Reson. Med. 1995; 34:604-611.

[36] Doty FD. MRI Gradient Coil Optimization. In: Blumler P, Blumich B, Botto R, Fukushima E, editors. Spatially Resolved Magnetic Resonance: Methods, Materials, Medicine, Biology,

Rheology, Geology, Ecology, Hardware. New York:Wiley-VCH; 1999. p 647-674.

Figure Captions:

FIG. 1. Plots of (a) gradient coil efficiency, (b) inductance, and (c) average temperature rise, as functions of radius for five different fixed values of maximum winding density. The hypothetical body coil design upon which all the scalings are based is indicated by the cross and the effective radius of the proposed mouse coil is represented by the vertical line. The position of the target efficiency (a) and maximum allowed inductance (b) are indicated by the horizontal lines on the respective plots.

FIG. 2. Schematic diagrams of the temperature variation during (a) burst mode and (b) continuous mode operation. Solid vertical bars at the bottom of each diagram represent the acquisition of a single EPI image.

FIG. 3. Schematic diagrams of five layer, three axis coils interleaved in (a) unbalanced and (b) balanced configurations.

FIG. 4. Photograph of gradient coil prior to addition of outer cooling layer. Electrical jumpers connect layers within the X and Y axes in series. Six free brass electrical connections (two per axis) are visible at the top of the coil. Four thermocouple connectors are visible at the front of the top surface. The 1cm aperture through the side is visible halfway up the front of the coil.

FIG. 5. Contour plot of the efficiency [mT/m/A] of the innermost transverse layer (radius = 2.775cm) over axes of coil length and 30% ROU size. The position of the chosen transverse layer

design is indicated by the star. The vertical line marks the minimal allowed ROU size for mouse imaging.

FIG. 6. Single octant wire patterns for the (a) transverse and (b) longitudinal axes. Arrowheads indicate relative direction of current within each pattern. A region of current reversal is present on the longitudinal (z) axis only. The pattern in (a) is used for all transverse layers within the coil, shifted by ninety degrees for the y axis layers. The maximum winding density on the transverse and longitudinal patterns are $8cm^{-1}$ and $10cm^{-1}$, respectively.

FIG. 7. Measured temperatures at the region of highest wire density on the X-axis over time while passing 20A DC through the X-axis alone. Heating was stopped when the maximum temperature increased by 30°C. The solid triangles represent the response with no cooling applied, wheras the solid diamonds represent the response with 4l/min water cooling. The solid lines are the results of fitting equation (5) to the measured data. The response of the Y and Z axes were similar.

FIG. 8. The number of single shot EPI images ($N_p = 64$, $N_r = 64$, SW = 500kHz, V = 400V, $\Delta T_b = \Delta T_{rms} = 10°C$, water cooling = 4l/min, and η_r, L_r, R, and k_h equal to the values for each axis as

given in tables 2 and 4) that can be collected by each axis during a single burst period, as a function of field of view.

FIG. 9. The minimum TR for a single shot EPI image (N_p = 64, N_r = 64, SW = 500kHz, V = 400V, $\Delta T_c = 10°C$, water cooling = 4l/min, and η_r, L_r, R, and k_h equal to the values for each axis as given in tables 2 and 4) for continuous mode scanning, as a function of field of view.

FIG. 10. Gradient echo image of a grid phantom collected with the mouse gradient coil at 4T. Imaging parameters were: TR / TE / flip angle = 50ms / 4ms / 11°, number of averages = 16, FOV = 4 x 4cm^2, matrix = 256 x 256, resolution = 156 x 156 x 2000μm^3, collection time = 3min 24sec. The image has been cropped to highlight the phantom of size 26 x 26mm^2. Dark squares within the grid are 2 x 2mm^2 and are separated by 2mm. The dashed box represents an area 10 x 10mm^2 within which the gradient is uniform to better than 1%.

FIG. 11. Fast spin echo image of an excised rat brain collected at 1.5T. Imaging parameters were: TR / TE = 3500ms / 18ms, echo train length = 4, number of averages = 24, FOV = 17 x 17mm^2, matrix = 256 x 192, resolution = 65 x 87 x 625μm^3, collection time = 1hr 15min. The smooth, round outer surface of the brain is due to the 14mm diameter tube into which the brain was placed during imaging.

Table 1: Summary of Calculated Results for Individual Layers

	radius [cm]	σ_w [cm^{-1}]	η [mT/m/A]	L [μH]	R [mΩ]
layer 1	2.775	8.3	7.8	12	67
layer 2	3.475	8.1	6.1	23	104
layer 3	4.175	10.0	11.0	97	200
layer 4	4.875	7.8	4.2	60	201
layer 5	5.575	8.2	3.9	98	275

Table 2: Calculated Results for Interleaving Combinations

	η [mT/m/A]			L [μH]		
	GX	GY	GZ	GX	GY	GZ
XXYYZ	13.9	9.2	8.2	60	161	231
XYXYZ	12.8	10.3	8.2	64	114	231
XYYXZ	12..1	11.1	8.2	84	102	231
XXYZY	13.9	8.9	9.4	60	182	154
XYXZY	12.8	10.0	9.4	64	141	154
XYYZX	11.7	11.1	9.4	121	102	154
(a) XXZYY	13.9	8.1	11.0	60	259	97
XYZXY	12.1	10.0	11.0	84	141	97
(b) XYZYX	11.7	10.3	11.0	121	114	97
XZXYY	12.8	8.1	13.2	64	259	56
XZYXY	12.1	8.9	13.2	84	182	56
XZYYX	11.7	9.2	13.2	121	161	56
ZXXYY	11.1	8.1	16.5	102	259	28
ZXYXY	10.3	8.9	16.5	114	182	28
ZXYYX	10.0	9.2	16.5	141	161	28

Table 3: Calculated Values for Increased Number of Layers

	η [mT/m/A]			L [µH]		
	GX	GY	GZ	GX	GY	GZ
XYZYX	11.7	10.3	11.0	121	114	97
XYZYX**XYZ**	15.1	13.4	18.9	419	396	1064
XYZYX**XZY**	15.1	13.1	19.7	419	444	891
XYZYX**YXZ**	14.7	13.7	18.9	445	363	1064
XYZYX**ZXY**	14.7	13.1	20.1	445	444	701
XYZYX**YZX**	14.4	13.7	19.7	488	363	891
XYZYX**ZYX**	14.4	13.4	20.1	488	396	701

Table 4: Calculated and Measured Electrical Values

	L [µH]			R [mΩ]		
	calc.	1kHz	10kHz	calc.	1kHz	10kHz
layer 1	12	11.9	11.8	67	90	96
layer 2	23	23.0	23.0	104	124	131
layer 3	97	98.0	97.5	200	238	260
layer 4	60	61.0	61.0	201	262	273
layer 5	98	101.0	101.0	275	323	345
X axis	121	126.3	126.1	342	412	429
Y axis	114	118.4	118.2	305	380	400
Z axis	97	100.0	99.7	200	238	254

Table 5: Fit Results for Heating Measurements

Axis	Flow	Phase	ΔT_{ss} [°C]	τ [s]	k_h [°C A^{-2}]
X	0l/min	heating	49	1053	0.297
		cooling	-11	236	
	4l/min	heating	34	666	0.204
		cooling	-31	665	
Y	0l/min	heating	51	786	0.332
		cooling	-17	317	
	4l/min	heating	40	631	0.274
		cooling	-31	649	
Z	0l/min	heating	37	768	0.388
		cooling	-17	253	
	4l/min	heating	21	430	0.228
		cooling	-22	256	

Figure 1

(a)

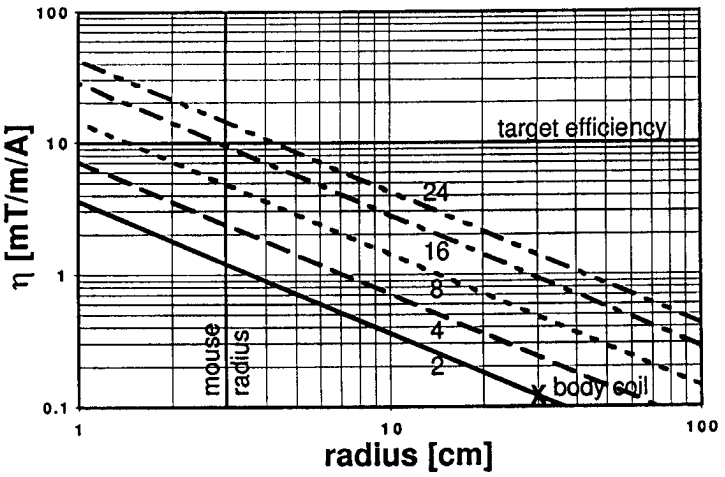
100
10
1
0.1
η [mT/m/A]
target efficiency
24
16
8
4
2
body coil
mouse radius
1
10
100
radius [cm]

(b)

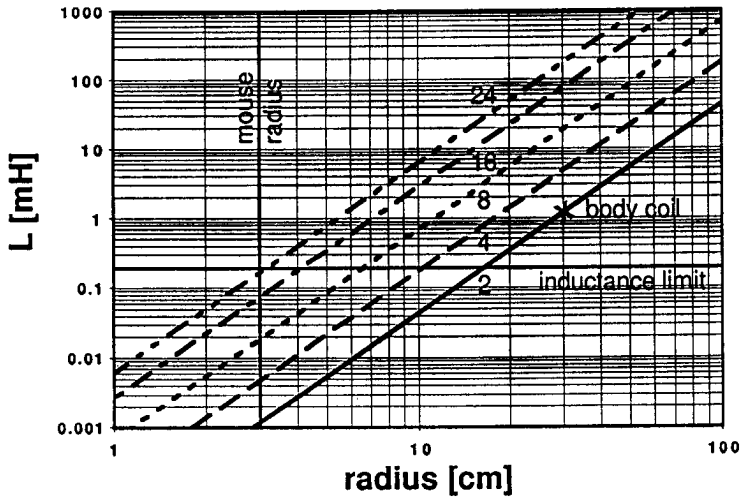
1000
100
10
1
0.1
0.01
0.001
L [mH]
mouse radius
24
16
8
4
2
body coil
inductance limit
1
10
100
radius [cm]

(c)

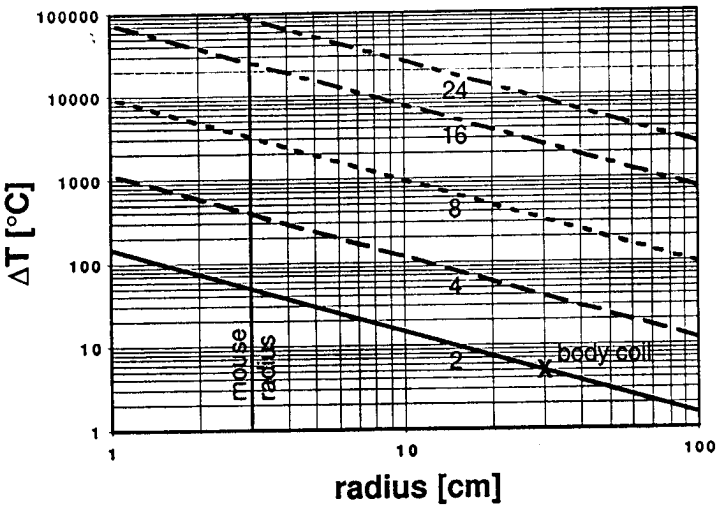
100000
10000
1000
100
10
1
ΔT [°C]
24
16
8
4
2
body coil
mouse radius
1
10
100
radius [cm]

Figure 2

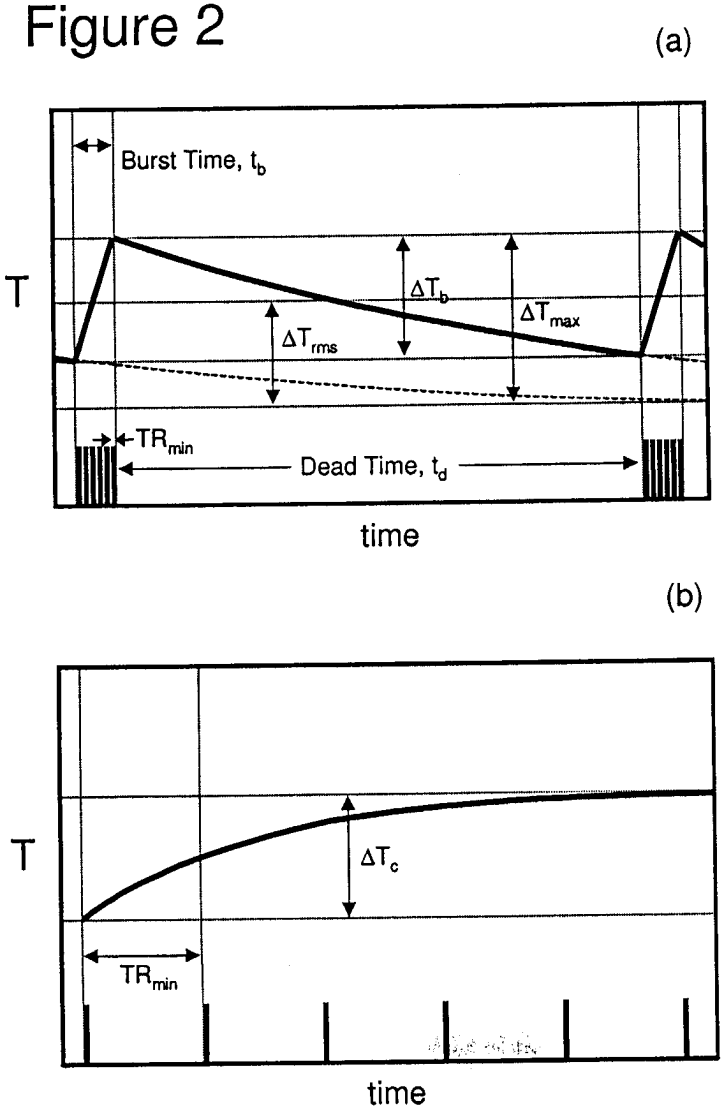

Figure 3

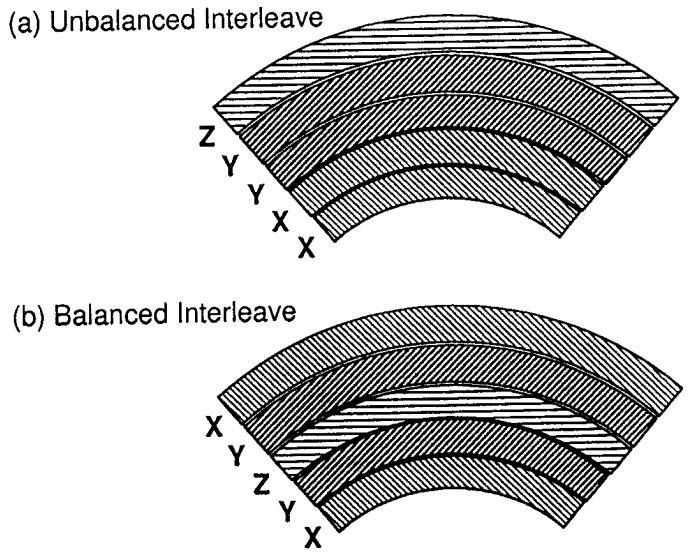

Figure 4

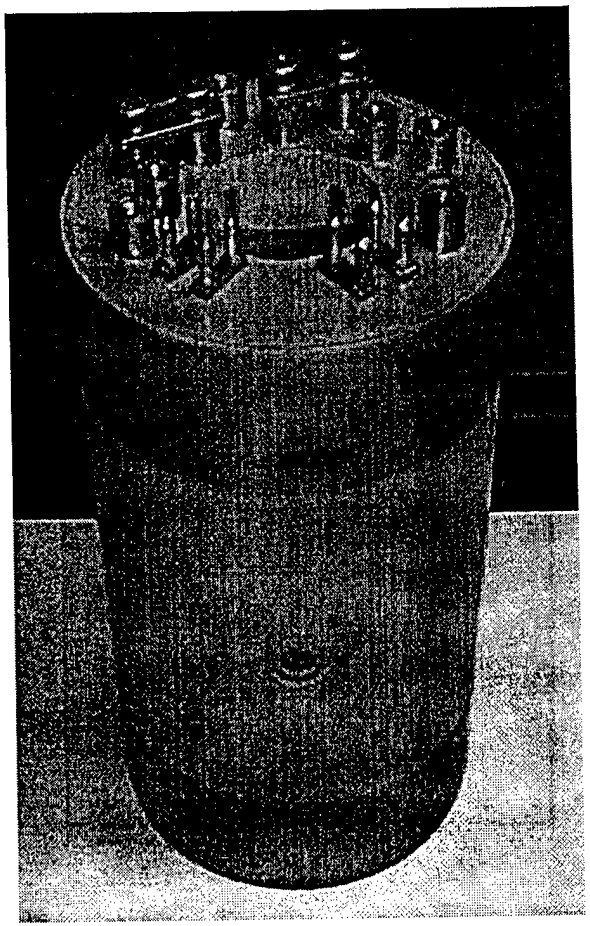

Figure 5

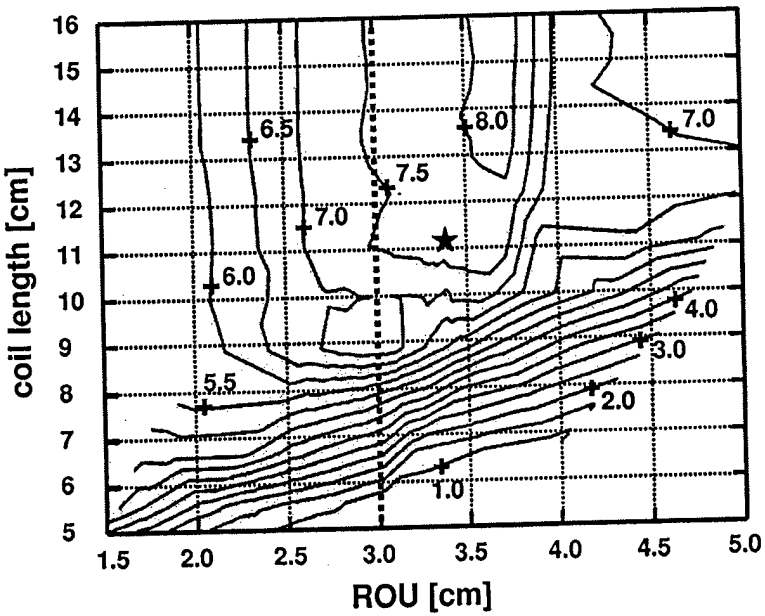

Figure 6

(a)

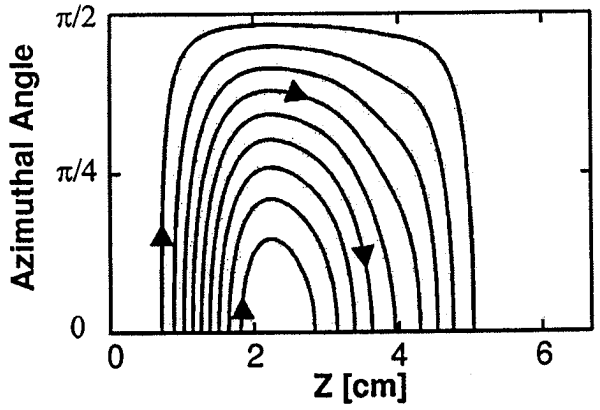

(b)

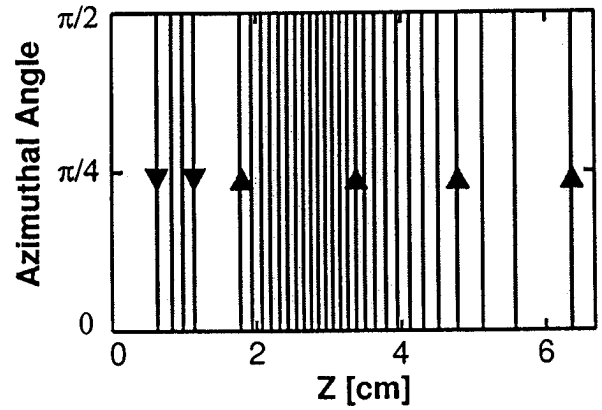

Figure 7

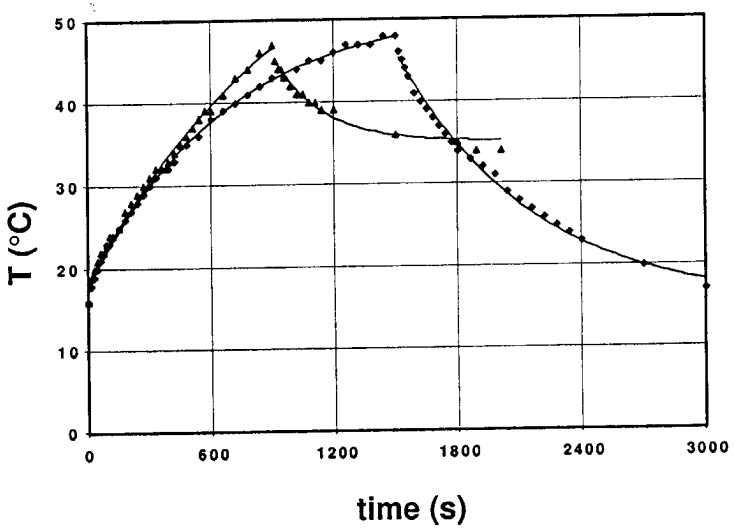

Figure 8

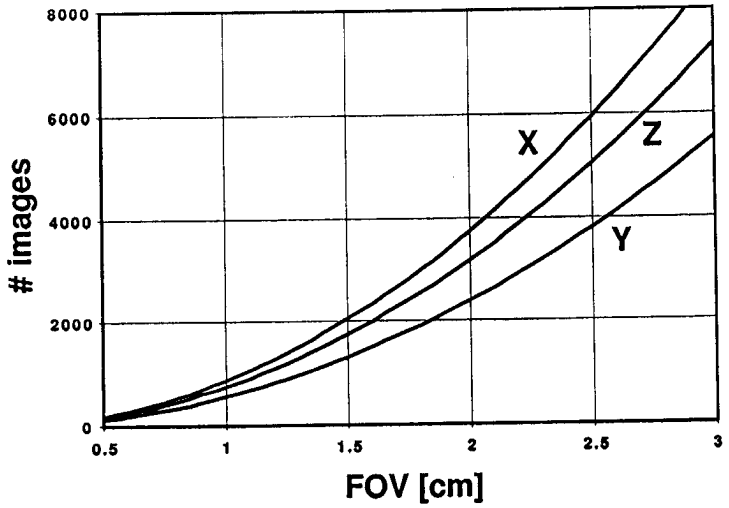

Figure 9

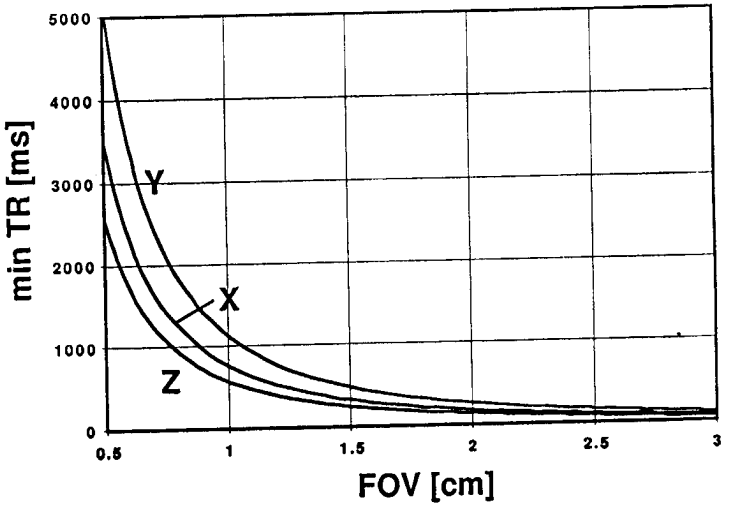

Figure 10

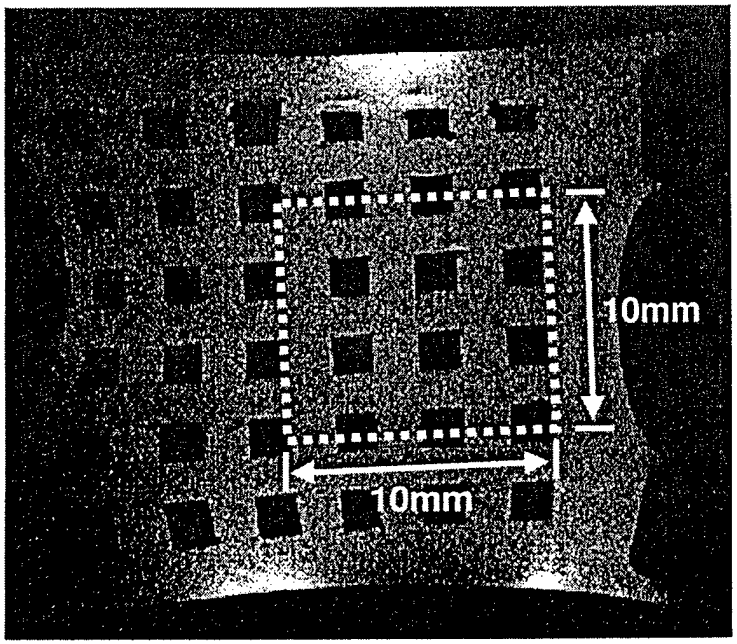

Figure 11

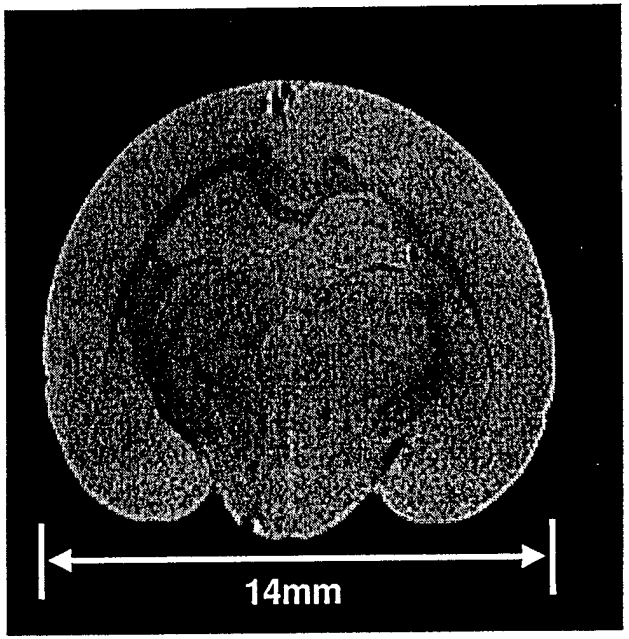

Appendix II

The IVIM method and the analysis program developed for this grant were tested with two substances – water and acetone - whose diffusion coefficients are well documented. The theoretical and experimentally determined results are shown below for diffusion encoding along six different directions:

Water:

The theoretical value of the diffusion coefficient of water is between 2.12×10^{-3} and 2.63×10^{-3} mm^2/s at 21.7 C°.

Diffusion Encoding Direction	Diffusion Coefficient (mm^2/s)
xy	$2.03 \pm 0.02 \times 10^{-3}$
-xy	$2.10 \pm 0.09 \times 10^{-3}$
xz	$2.08 \pm 0.10 \times 10^{-3}$
-xz	$1.97 \pm 0.06 \times 10^{-3}$
yz	$2.07 \pm 0.04 \times 10^{-3}$
-yz	$2.07 \pm 0.11 \times 10^{-3}$

Acetone:

The theoretical value of the diffusion coefficient of acetone is between 3.88×10^{-3} and 4.43×10^{-3} mm^2/s at 21.7 C°.

Diffusion Encoding Direction	Diffusion Coefficient (mm^2/s)
xy	$4.47 \pm 0.04 \times 10^{-3}$
-xy	$4.59 \pm 0.05 \times 10^{-3}$
xz	$4.62 \pm 0.03 \times 10^{-3}$
-xz	$4.30 \pm 0.05 \times 10^{-3}$
yz	$4.47 \pm 0.06 \times 10^{-3}$
-yz	$4.55 \pm 0.06 \times 10^{-3}$

Reference: Bammer R, *et al.* Diffusion-weighted imaging with navigated interleaved echo-planar imaging and a conventional gradient system. *Radiology* **211**:799 (1999).

Appendix III

Shown below are the bi-exponential diffusion coefficients before (D_A, D_B) and after (D_X, D_Y) cessation of blood flow (euthanasia) in non-necrotic regions of interest in low and high dose tumours.

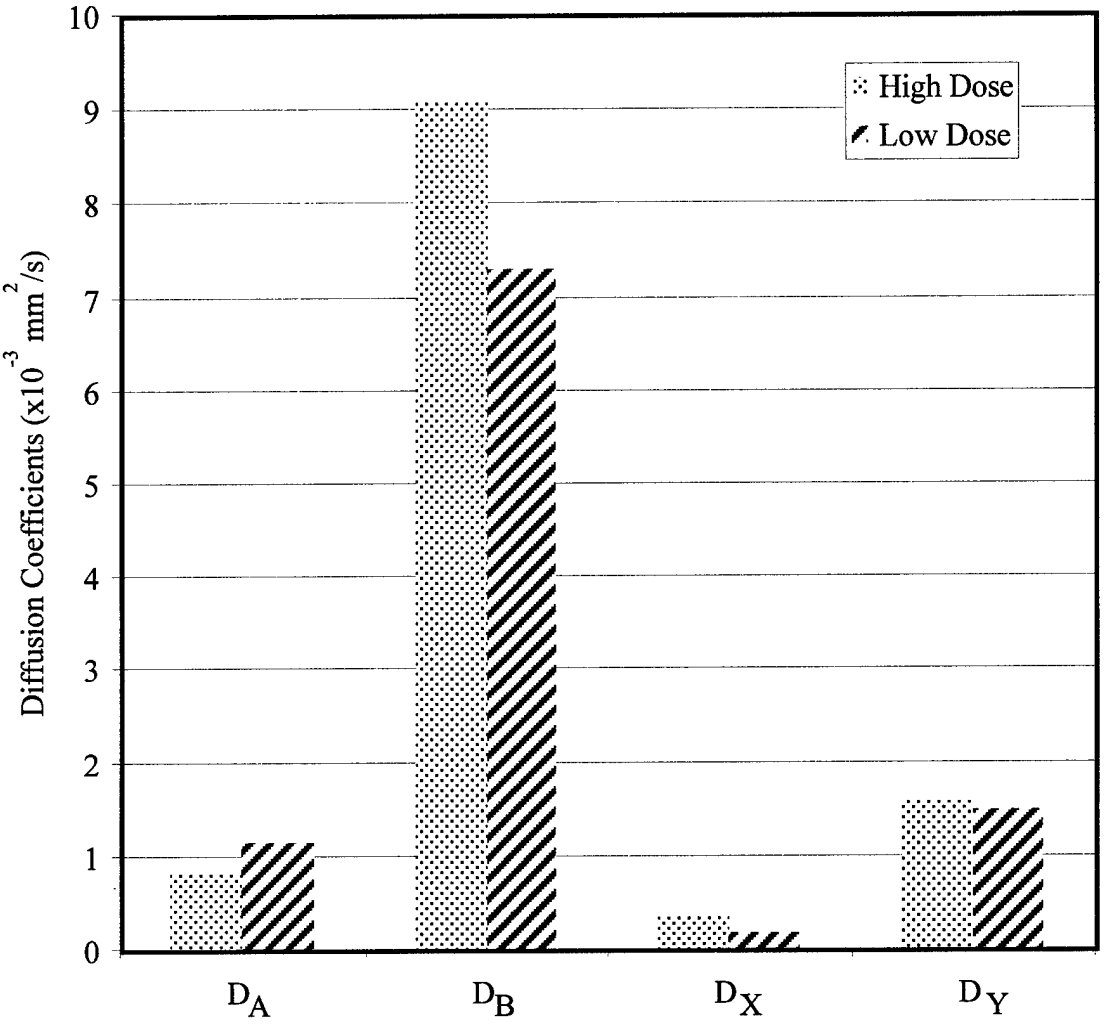

Note that the fast decay component (large diffusion coefficient), D_B, disappears post cessation of blood flow. The presence of a bi-exponential decay post cessation of blood flow may be attributed to different rates of diffusion in the intra- and extracellular spaces. We are currently endeavoring to assign these two diffusion components.

Practical Design of a High-Strength Breast Gradient Coil

Cynthia F. Maier, Hristo N. Nikolov, Kenneth C. Chu, Blaine A. Chronik, Brian K. Rutt

A high-strength three-axis local gradient coil set was constructed for MRI of the breast. Gradient fields with good uniformity (<10% deviation from the desired gradient) over most of the volume required for breast imaging were generated with efficiencies of up to 3.3 mT/m/A. The coils will allow diffusion breast imaging in clinically acceptable examination times. The electrical design, water cooling system, and fabrication techniques are described. Preliminary tests of the coil included images of a grid phantom and diffusion measurements in a short-T_2 agarose gel phantom.

Key words: breast imaging; diffusion imaging; gradient coils.

INTRODUCTION

In this paper, we present a specialized gradient coil design for breast imaging and demonstrate the utility of this coil for performing MR diffusion imaging with short-duration, high-strength gradient pulses. Sensitization of an MR pulse sequence to motion can be achieved using conventionally available gradient hardware; however, measurement of water diffusion (or slow flow in microvessels) with this hardware requires long echo times to achieve large gradient moments and therefore suffers from significant signal loss due to T_2 relaxation and system nonidealities. In addition, increasing the time between motion-sensitizing gradient pulses allows more macroscopic motion to occur in this interval, resulting in pixel misregistration, motion-induced ghost artifacts, and diffusion/flow measurement artifacts. Higher-strength gradients will allow adequate sensitization to small motions (i.e., large gradient moments) with very short, high-amplitude gradient pulses and minimal time delay between these pulses.

METHODS

The gradient coil assembly was designed in a cylindrical geometry, with each gradient coil built onto a separate cylindrical former. The three-axis coil set was composed of concentrically nested coils, oriented vertically such that their common axis was transverse to the main field as shown in Fig. 1. Space restrictions within the magnet bore require that the coils be as short as possible in the vertical direction to allow a patient to lie comfortably above the top edge of the cylinders. Unfortunately, decreasing the height of the coils (relative to their diameters) makes the creation of uniform gradients within the coils much more difficult. To satisfy the competing demands of good gradient uniformity and height restrictions, we used an aspect ratio of approximately 1:1 for our cylindrical coils. The height of the complete coil assembly was 16 cm, leaving 34-cm clearance in the vertical direction in our General Electric (GE) Signa Horizon scanner (General Electric Medical Systems, Milwaukee, WI), and the largest coil diameter was 21.6 cm.

To generate the winding densities required for high gradient strengths, relatively small-diameter wire (AWG no. 20) was used to construct the coils. The resistivity of this wire is high, requiring an active cooling system to remove heat and maintain temperatures inside the coils within a range comfortable for the patient. Water-cooling jackets with very thin walls were sandwiched between the gradient coils, so that resistive heat could be removed efficiently while maintaining the compact construction of the coil assembly. A dedicated RF coil and shield were mounted inside the innermost gradient coil with an approximately 1.3-cm space between the RF coil and closest gradient coil. The entire assembly is depicted in cross-section in Fig. 2.

Electrical Design

The highly efficient quadrupolar current distribution (1–3) was used to provide gradients in B_z along both the x and z directions (G_x and G_z). This current density varies azimuthally as $\cos(2\theta)$ and is entirely directed along the axial direction on the surface of the cylindrical former. Discrete wire positions approximating the continuous quadrupolar current density were calculated by sampling the current density $\cos(2\theta)$ at θ_i such that $\cos(2\theta_{i+1}) - \cos(2\theta_i)$ was constant. A schematic diagram showing this ideal wire distribution is given in Fig. 3a. The current pattern in Fig. 3a is nonphysical in that the current is discontinuous at the ends of the coil, and therefore, connecting paths between the wires ("return wires") must be provided. In most imaging applications in which local gradient coils have been used previously, the volume to be imaged has been located at the center of the coil, and placing return paths near the ends of the cylinder had a minimal effect on the desired field within the object. For breast imaging applications, the required location for the region of good gradient uniformity is near the top edge of the coils and a conventional return wire arrangement would corrupt the gradient field uniformity within this volume. We chose to place the return wire components instead on horizontal plates at the tops and bottoms of the coils. Close to the cylinders on the plates, the return paths were extended along the z direction for at least 5 cm (no B_z is generated by current in the z direction). The bottom set of return wires for the G_z coil were strung across the bottom of the cylinder in the z direction. The quadrupole current distribution for G_x is rotated 45° with respect to G_z, and the return wires for G_x could not be strung in the z direction; therefore, these wires were located on a horizontal plate.

MRM 39:392–401 (1998)

From the Departments of Medical Biophysics and Diagnostic Radiology, University of Western Ontario, London, Ontario, Canada; and Tom Lawson Family Imaging Research Laboratories, John P. Robarts Research Institute, London, Ontario, Canada.

Address correspondence to: B. K. Rutt, Ph.D., Department of Diagnostic Radiology, University Hospital, London, Ontario, Canada N6A 5A5.

Received March 10, 1997; revised August 21, 1997; accepted August 22, 1997.

This work was supported by the Breast Cancer Society of Canada and the Canadian Breast Cancer Research Initiative, National Cancer Institute of Canada. C.M. was supported by a W.T. McEachern Scholarship and by a U.S. Army Breast Cancer Predoctoral Fellowship.

0740-3194/98 $3.00

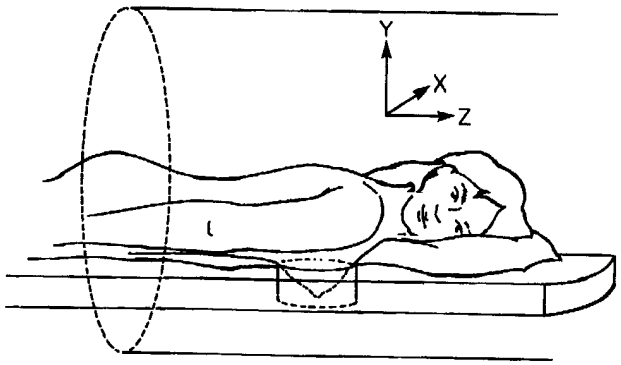

FIG. 1. Schematic showing orientation of local breast gradient coil in magnet.

The design of the G_y gradient makes use of the fact that $\nabla \times B = 0$ throughout any region in which the current density is 0. This means that a transverse gradient coil with its axis along z (the conventional orientation) can be turned 90° about the x axis so that its axis is along the y direction and used to produce a gradient in B_z along the y direction. We designed a transverse gradient coil in the conventional orientation using the target field method (4, 5) and then rotated the coil to produce G_y. Although a wide range of breast sizes exist, we defined an average volume of interest (VOI) for breast imaging (by comparison with commercially available breast RF coils) as a cylindrical volume with length equal to 60% of the coil height (11.5 cm), a diameter equal to 90% of the RF coil diameter (13.5 cm), and location flush with the top surface of the gradient coil assembly. The target field coil was designed to have its region of good gradient uniformity centered on this VOI. This design consisted of only two sets of closed current loops (Fig. 3b). For the target-field coil in its conventional orientation with its axis along z, the desired gradient is created almost entirely by the current in half of the wire loops only (the "primary" component of the loop as indicated in Fig. 3b), and return wires are an intrinsic part of the design (labeled "return" in Fig. 3b). For this coil, only one set of "return paths" is required for current continuity, and in the vertical orientation, these wires are located at the bottom of the cylinder. In our coil design, such a large number of loops was required to generate the desired gradient efficiency that these return wires would have occupied a large fraction of the space available on the surface of the cylinder. Due to the strict limitations on coil height, we believed that this space could be used more efficiently if only the primary component of the coil design was present on the cylinder itself and the return paths were located on a horizontal plate as for the quadrupole coils. A complication that arises from truncating the wire pattern in the vertical dimension in this way is that the reciprocity relations from Maxwell's equations no longer hold for a nonphysical current distribution (i.e., $\nabla \times B \neq 0$ for a current distribution with nonzero divergence). This means that the gradient field calculated for the truncated design is not identical in the conventional and transverse orientations unless the return wires are included in the calculation. We shall see in the Results section that the truncated coil in the transverse orientation has both an increased gradient efficiency compared to the full design for the same coil height and, additionally, the region of acceptable gradient uniformity (<20% deviation from uniformity) is significantly larger for the truncated coil.

One undesirable side effect that arises from locating the return wires on horizontal surfaces is that the torque on the coils from interaction with the main static field is greatly increased. This effect is significant. For our 1.5-T

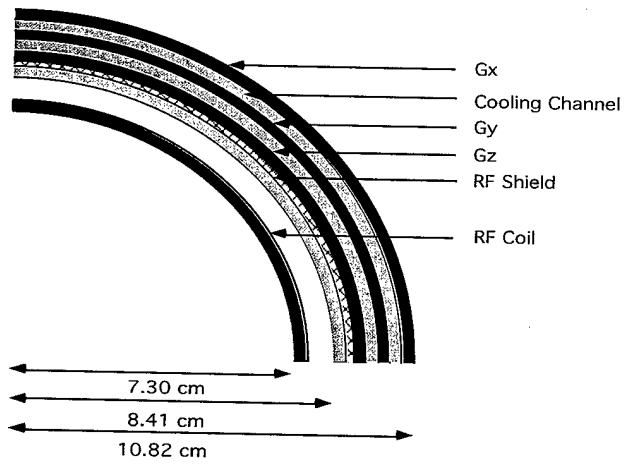

FIG. 2. Cross-section of complete gradient coil assembly showing location of RF coil and water-cooling modules.

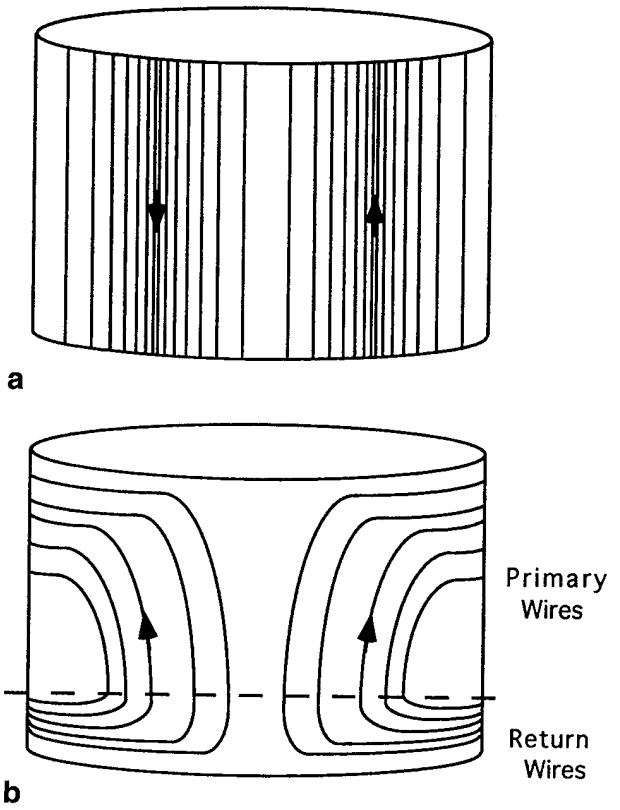

FIG. 3. (a) Quadrupolar current density with 56 windings. (b) Target-field-design transverse coil. The "primary wire" component is almost entirely responsible for generation of the transverse gradient for the conventional coil orientation with its axis along z.

magnet, current is only supplied when the coils are positioned near the central, highly homogeneous region of the magnet (typical clinical imaging systems have a 50-cm-diameter spherical volume of better than 10 ppm B_0 uniformity) and the upward (downward) force on the $+z$ ($-z$) half of the horizontal plate for the G_z coil is approximately 15 N/A (3.5 lb/A) increasing linearly with applied current. As the gradients are switched, the effect of this force is to create an alternating torque of approximately 3 Nm/A in size. For many pulse sequences, the direction of the current is switched rapidly, resulting in a torque that alternates direction rapidly and causes significant vibrational stress on the coils. For our preliminary experiments, a temporary coil support was constructed from wood- and glass-reinforced phenolic. The horizontal plates were rigidly attached to the support, and the support structure itself served to mount the coil assembly inside the bore of the imager, thereby preventing any bulk coil motions that could arise from the magnetic forces on the wires. The wires themselves were potted securely in the milled grooves using epoxy and were prevented from vibrating loose from these grooves by the next adjacent layer of cooling channels, since all layers were tightly sandwiched together.

Coil Construction

To produce high gradient efficiencies, it is advantageous to use the maximum number of wires possible. This number is constrained in an obvious way by the wire diameter, minimum spacing between wires, and circumference of the cylindrical former. To obtain the desired gradient efficiencies for these coils, it was necessary to use relatively small wires (AWG no. 20) with a diameter of ~1 mm and an interwire spacing of 0.5 mm. The G_x (outermost) coil was wound with a single length of wire such that 216 axially directed segments generated the required current density, and for the G_z (innermost) coil, 200 axially directed segments were wound. For the middle coil (G_y), constraining the closest separation of the wires to be 0.5 mm allowed 48 loops per side. For all three coils, the wire paths were milled (numerically controlled) into the surface of polycarbonate/acrylic formers. Wire was then wound into these grooves and epoxied in place. Figure 4a shows the constructed G_x coil, complete with horizontal plates after winding with (dielectric) insulated copper wire. The upper plates were curved downward at the superior and inferior ends to provide a more comfortable structure for patient support. Figure 4b shows the middle coil (G_y) before assembly of the complete gradient coil unit.

The resistivity of the small-diameter wire used to construct the coils is relatively high, increasing from 33.3 mΩ/m at room temperature to 40.5 mΩ/m at 75°C (our specified upper limit on temperature at the wire). The additional length of wire required to extend the return paths away from the main cylinders also contributed to high coil total resistances. Since high root-mean-squared (RMS) currents are required for the desired imaging applications, the power dissipated by the coils is significant (~1250 W for one coil @ 25A RMS). In a mock-up of one quadrant of a coil, when a 25A RMS current was applied with no cooling, the temperature of the quadrant rose from 10°C to 100°C in 2.5 minutes. With air cooling only, a temperature rise from 10°C to 35°C in 4 minutes was observed. A more efficient cooling system was therefore required to ensure patient safety.

Water is one of the most efficient and economical cooling fluids available. Its heat capacity (C_p = 4.18 J/g/°C) is approximately two times higher than other commonly available cooling fluids such as hydrocarbon oils (e.g., ethylene glycol). Assuming that all heat generated is transferred to the cooling water and the maximum allowable temperature rise of the water is 5°C, a water flow of 3.6 liter/min is required to remove 1250 W of heat. Conventionally, water-cooling channels for gradient coils are constructed from copper tubing. For a compact gradient coil set, the competing demands of space limitations and the requirement of a large cooling channel cross-section to ensure adequate volume flow rates necessitated the design of a novel cooling system. We designed this cooling system in separate modules, each module corresponding to a quadrant of a single gradient coil. Each module consisted of a skeleton of cooling channel spacers that were milled from a 3.0-mm-thick polycarbonate sheet. This was covered on both sides with a very thin (0.25-mm-thick) polycarbonate film (GE Plastics, General Electric Company, Pittsfield, MA) to allow close thermal contact of the wires with the cooling water while ensuring electrical insulation. The film was bonded to the skeleton using ultraviolet-curing polyvinyl chloride-based bonding adhesive (Loctite 3311, Loctite Corporation, Mississauga, Canada). The tensile strength (to break) of the polycarbonate film was rated at 9000 psi, according to American Standards of Testing Materials (ASTM) D882, and the burst strength was 200 psi (ASTM D774). The modules were tested for flow uniformity and resistance to leaks by flowing water at 13 liter/min for >5 hours before permanent incorporation into the gradient coil structure. After incorporation into the gradient coil set, the modules were connected in parallel to lower the fluid resistance of the network of cooling channels and thereby allow increased water flow rates.

This design allowed very close thermal contact between the wires and water in the cooling channels (while maintaining electrical isolation) and also provided a large surface area over which heat could be transferred to the water. The ability to test the cooling channel integrity separate from the gradient coil structure was vital in ensuring no electrical shorting due to water leakage. An additional benefit of constructing the cooling system from polycarbonate is that no electrical currents can be created in this material, and it is therefore not susceptible to eddy current generation like some copper systems. Since the thickness of the cooling channel module was only 3.5 mm, the maximum total wall thickness of the gradient coil structure was less than 3 cm. The assembled gradient coil structure, including RF coil and water connections, is shown in Fig. 5.

RF Coil

Several cylindrical RF coil designs exist that can be used in a transverse geometry for imaging the breast (i.e., with

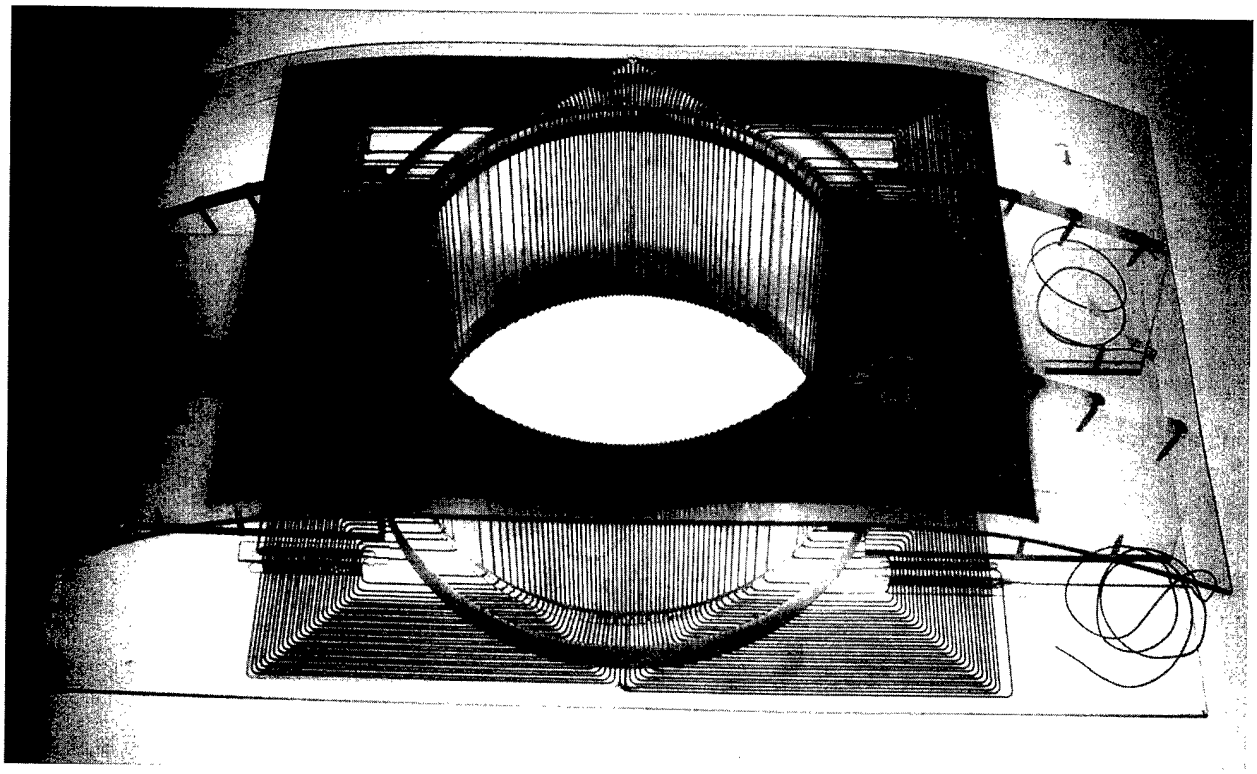

a

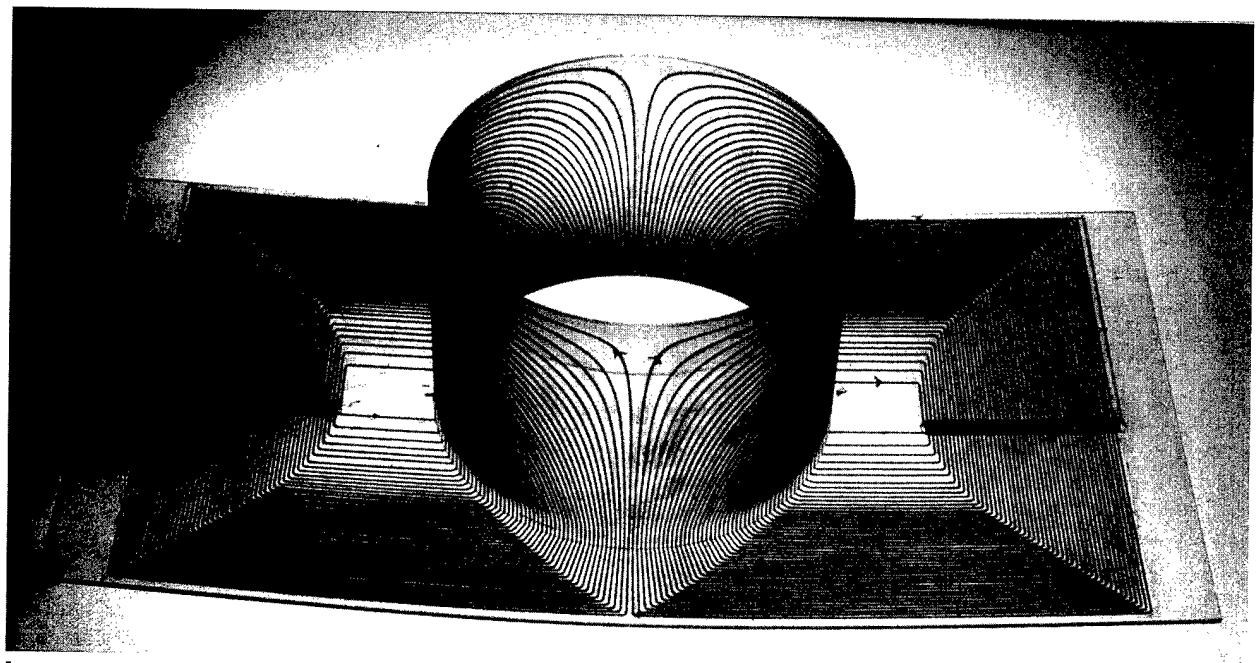

b

FIG. 4. (a) G_x quadrupole coil with 216 windings. (b) G_y coil showing placement of the "return wires" on a horizontal plate.

the coil axis perpendicular to the main magnetic field B_o). These coils, when oriented vertically, produce B_1 fields directed along either the horizontal x direction (e.g., saddle coils (6)) or along the vertical direction (e.g., solenoidal coils (7, 8)).

The construction of an RF coil for operation inside our breast gradient coils is a difficult problem, in that the proximity of the RF coil to the gradient coils results in very strong inductive coupling and detuning of the RF coil (given that the gradient coil radius is constrained to be as small as possible for maximum efficiency). To determine the best RF coil design for our gradient coil set, two different RF coils were constructed and tested. The first coil constructed was a quadrature RF coil with

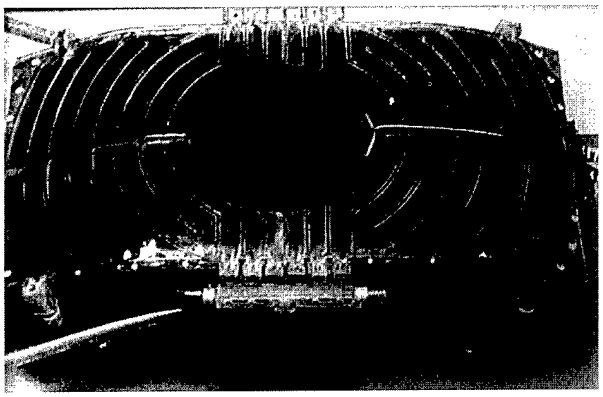

FIG. 5. Assembled gradient coil module showing RF coil and cooling channels.

two separate coils providing the perpendicular B_1 components. In this arrangement, a simple three-loop solenoidal coil provided the vertical mode, and a saddle coil built onto the same former provided the horizontal mode. The second coil constructed was a 16-rung high-pass birdcage RF coil designed for operation in a linear mode (recall that a birdcage coil cannot be used in quadrature mode in the vertical orientation because one of the modes would be parallel to B_0). We chose this design over a saddle-coil arrangement because of the superior uniformity of B_1 produced by the birdcage coil over the volume enclosed by the coil. A split cylindrical RF shield was constructed from fine copper screen and located immediately inside the smallest diameter gradient coil. The coils were tested for coupling to the gradient coils. The quality factors, Q, were measured, and the coil performances were compared.

Diffusion Imaging

Preliminary diffusion measurements were made using a short-T_2 phantom consisting of $NiSO_4$-doped agarose gel (T_2 = 60 ms at 1.89 T) with a diffusion-sensitized spin-echo sequence (pulsed gradient spin-echo sequence (9)). Apparent diffusion coefficient (ADC) maps were calculated from a series of 10 diffusion-weighted images with diffusion b factors between 0 and 1000 s/mm^2. Each of these images was the geometrical average of two images with equal diffusion-weighting but with opposite diffusion gradient polarity to remove the effects of diffusion-weighting cross-terms from interaction between the diffusion and imaging gradients (10). The ADC maps were obtained under three conditions: (1) using the standard whole-body manufacturer-supplied gradient coils for all imaging and diffusion-weighting gradients; (2) using our custom coils for all imaging and diffusion-weighting gradients, with the gradient strengths matched to those of the whole-body coils by applying an appropriately scaled current to the coils; and (3) using our custom coils for all imaging and diffusion-weighting gradients, with the imaging gradient strengths matched to those of the whole-body coils, but taking advantage of the increased gradient efficiency to apply higher strength, shorter diffusion-weighting gradients, thereby shortening the scan TE. In the first two experiments, the minimum TE required for diffusion weighting of b = 995 s/mm^2 was TE = 80 ms (with diffusion gradient strength of 22 mT/m). TR was set to 600 ms, the matrix size for the scan was 256 × 128, and the image size was 8 × 8 cm, for a total scan time of 2.5 minutes for each image (5 minutes for each b factor). Diffusion gradients were applied along the readout axis, x, for all experiments. For the third experiment, the TE was decreased to TE = 46 ms by increasing the strength of the diffusion-weighting gradient pulses by a factor of four (88 mT/m) to obtain much larger b factors with shorter diffusion pulses. All other parameters (including slice thickness) were matched to the first two experiments.

RESULTS

Coil Performance

The field produced by each of the three coils was calculated by direct numerical solution of the Biot-Savart Law for the wire paths, including return wire contributions. Calculated gradient efficiency for all three coils, together with the measured resistance and inductance, are summarized in Table 1. Contour plots of calculated gradient uniformity for the G_z quadrupole coil are shown in Fig. 6. Figure 6a shows the percentage deviation from gradient uniformity for a y-x plane through the center of the coils. A similar plot is shown in Fig. 6b for a x-z plane, transverse to the coil axis, at a height equal to the center of the VOI (i.e., located 5.9 cm below the top surface of the coils). These plots show the excellent gradient uniformity within the VOI that is predicted for the G_z coil. The gradient strength decreases near the ends of the coil, because the finite length of the coil causes a decrease in field strength. Similar results were obtained for the G_x gradient coil, with appropriate scaling for the number of wires and the coil radius. The performance of the modified target field G_y coil is shown in Figs. 6c and 6d. A larger deviation from gradient uniformity is present for this coil, compared to the G_x and G_z coils. This problem is inherent to any design for a G_y coil in the transverse orientation, since there is an additional gradient in the y direction due to the natural field fall-off that occurs as the ends of the coil are approached. To create a G_y coil with optimum gradient efficiency, we would like to maximize $|B_z|$ at both ends of the coil, with B_z a maximum in the $+z$ direction at one end of the coil, and a maximum in the $-z$ direction at the opposite coil end. The field fall-off inherent in this coil orientation works against the gradient we desire to create, since it necessarily results in a decrease in the magnitude of B_z as the coil ends are approached. Instead of working against the natural field fall-off toward the ends of the coil, we have designed a

Table 1
Coil Performance Characteristics

	Mean diameter (cm)	Efficiency (mT/m/A)	Inductance (μH)	Resistance (Ω)
G_x (quadrupole)	21.1	2.9	754	2.3
G_y (fingerprint)	19.5	1.7	829	2.6
G_z (quadrupole)	18.1	3.3	1024	1.9

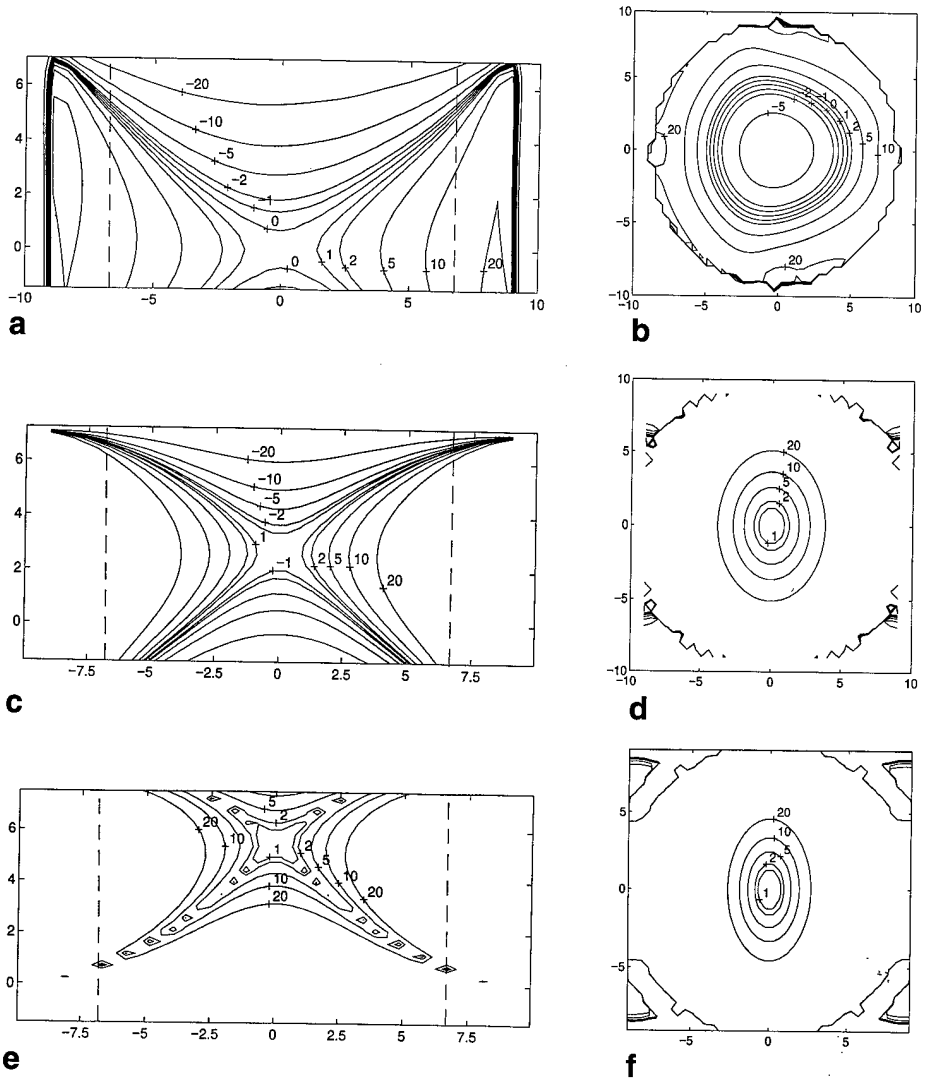

FIG. 6. Contour plots showing percentage deviations from gradient uniformity for the G_z coil over (a) an axial plane (x-y) showing the entire VOI with the top edge of the plot corresponding to the top surface of the coils. The outer circumference of the VOI is at 6.75 cm, as indicated by dashed lines. (b) A coronal plane (x-z) located at the center of the defined VOI, i.e., at ~3 cm above the geometric coil center. In Fig. 6a, the contours are symmetric around $y = 0$ cm with some small deviations due to return-wire contributions. (c, d) The corresponding plots for the constructed G_y coil shown in Fig. 4b. (e, f) The corresponding plots for a conventional transverse coil with return wires on the cylinder, as in Fig. 3b.

coil to produce $B_z = 0$ at the upper end of the coil, and a maximum in B_z toward the bottom end, similar to the asymmetric head coil design by Roemer (11). We used the target field approach to optimize the rate at which the field falls off toward the upper end of the coil to produce a linear variation in B_z. Although the region of acceptable gradient uniformity for our truncated target field coil is not as large as for the quadrupole coils, it compares favorably to the performance of the full target field design. We show in Figs. 6e and 6f the corresponding plots from a complete 40 loop per side target field coil with the same dimensions as our modified coil (i.e., with return wire paths at the bottom of the cylinder as in Fig. 3b). The region of acceptable gradient uniformity for our truncated target field coil is much larger than for the complete target field coil. In addition, the gradient efficiency is better for our truncated coil by a factor of 1.7, due to the larger number of windings that could be placed on the cylinder for our coil.

To verify the field simulations, gradient uniformity was tested by acquiring images of grid phantoms. Deviations from gradient uniformity are manifest in the images as geometric distortions. The phantoms consisted of acrylic cylinders filled with square plastic gridding and $CuSO_4$-doped 0.9% saline solution. The grid spacing was 1.7 × 1.7 cm, whereas the phantoms had an outer diameter of 12.5 cm and a height of 15 cm (extending 3 cm higher than the top surface when placed inside the coils). The coil performance was tested on a clinical GE Signa imager, using our coils for all imaging gradients (with gradient strengths matched to the whole-body coils) in a standard spin-echo pulse sequence. In general, local gradient coils often require modification of the compensation network for the gradient coil amplifiers since the

coil inductances are quite different from the whole-body coils. Because the inductances of our breast coils were very similar to the whole-body coils, no modification of the network was necessary. Images of a grid phantom are shown in Fig. 7 for planes corresponding approximately to the theoretical field plots shown in Figs. 6a and 6b and are evidence of the good gradient uniformity achieved over most of the VOI. These images were acquired using a spin-echo sequence with TE = 20 ms, TR = 500 ms, matrix size = 256 × 256, and 2 NEX. The image size is 16 × 16 cm, and the VOI vertical extent is marked with arrows.

The first RF coil we constructed was a quadrature coil consisting of a solenoidal coil to provide the vertical mode and a saddle coil to provide the horizontal coil. Unfortunately, the vertical mode was inductively coupled to both the *y*-gradient coil and to the RF shield and could not be tuned to the proton resonant frequency at 1.5 T. We therefore chose to construct a coil that would operate in linear mode, with only a horizontal B_1 component present. We constructed a birdcage coil that creates a horizontal mode B_1 field with a high degree of homogeneity over a large volume. The unloaded Q of this coil (when located inside the gradient coil structure) was 80, whereas the Q for loading with a 0.9% saline phantom was 29.

Although the gradient strengths required for conventional imaging (10 mT/m) can be generated at less than 6 A using these coils, higher currents are required for more demanding applications such as flow imaging and diffusion imaging. To test the effectiveness of the water cooling system, a DC current was applied to the coil with the highest total resistance, G_y, and the temperature rise was measured for different water flow rates by monitoring a thermocouple located on the surface of the wires. The temperature was monitored until equilibrium was achieved. Measured temperature rises are shown in Fig. 8 for DC currents between 0 and 22 A and a cooling water flow rate of 8 liter/min. Similar results were obtained for other flow rates, at which the equilibrium temperature increased with decreasing flow rates but did not change significantly from the results shown in Fig. 8 for higher flow rates. This behavior has also been demonstrated in purely cylindrical gradient coils and was modeled by Chu and Rutt (12) using an analysis based on fundamental heat transfer theory.

Diffusion Imaging

ADC maps for a T_2 = 60 ms $NiSO_4$-doped agar phantom are shown in Fig. 9; Fig. 9a shows the results obtained using the GE gradient coils, and Fig. 9b shows the results obtained using our gradient coils with diffusion gradient strengths four times higher than that of the GE coils. The mean ADC for all three experiments was the same within experimental error: $(1.8 \pm 0.3) \times 10^{-3}$ mm^2/s for the GE coils (±30% peak-to-peak), $(1.8 \pm 0.3) \times 10^{-3}$ mm^2/s for our gradient coils with diffusion gradient strengths matched to the GE coils, $(1.9 \pm 0.2) \times 10^{-3}$ mm^2/s for our gradient coils with diffusion gradient strengths four times higher than that of the GE coils and TE = 46 ms. As expected, the observed signal-to-noise ratio was increased by nearly a factor of 2 for the TE = 46 ms images compared to the corresponding *b*-factor images at TE = 80 ms.

DISCUSSION

The performance and homogeneity of the gradient coils were in excellent agreement with theoretical predictions. The volume of acceptable gradient uniformity (<20% deviation) extended over most of our defined VOI for all

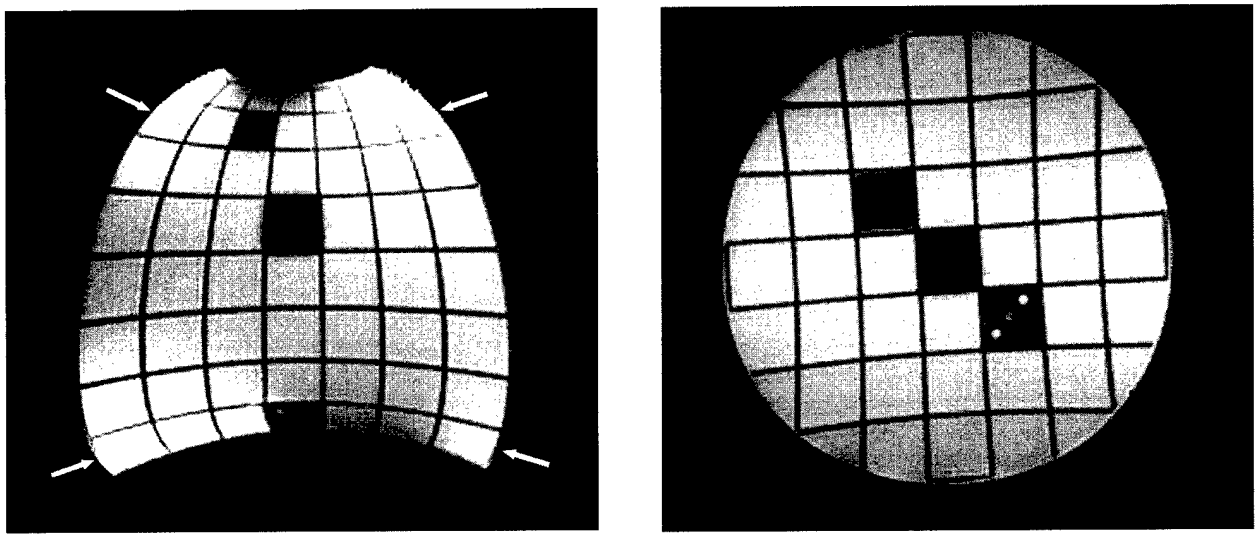

FIG. 7. Spin-echo images of a grid phantom acquired (a) for an axial plane (*x-y*) and (b) for a coronal plane (*x-z*) with the specialized breast quadrupole gradient coils. The input current strength required for the least efficient (G_y) coil was approximately 14 times less than that required for the corresponding GE coil.

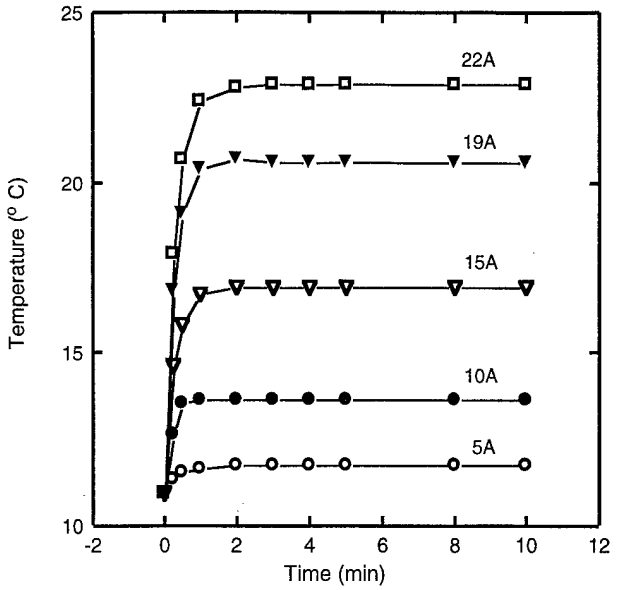

FIG. 8. Temperature response of assembled gradient coils to a DC current applied to the coil with the highest resistance (G_y) monitored at the surface of the G_y coil where the winding density was greatest.

three gradient coils. For this region, the theoretical plots of B_z can be used to generate a gradient-warping algorithm for the coils (13) to correct spatial distortions in the images. Additionally, the known deviations from gradient uniformity can be used to correct calculations of diffusion-weighting b factors (which will vary spatially across the VOI for our coils). Unfortunately, greater deviations from uniformity could not be avoided for the top 1 cm of the VOI near the upper edges of the coils for our coil designs. Deviations from uniformity of more than 20% lead to large image distortions and likely cannot be satisfactorily corrected using conventional schemes. Many breast lesions occur close to the chest wall; to be clinically useful, it is important to image accurately as close to the chest wall as possible. Several new gradient coils with improved gradient uniformity at the top edge of the coil have been reported recently (14, 15). Future improvements on our coil design will focus on extending the region of usable gradient beyond the top edge of the coil (16) as far as possible. For our preliminary clinical work with these coils, we will limit our study to patients with known lesions occurring in a region of the breast that falls within the 20% uniformity region of our gradient coils. This approach will allow us to implement pulse sequences under ideal conditions, (a) to determine the best parameters for visualizing breast lesions, (b) to determine the minimum required gradient strengths and uniformities, and (c) to make an initial assessment of the clinical utility of this approach.

In future coil designs, it may be possible to extend the region of usable gradient farther into the cylinder in the $-y$ direction by recessing the coils in the patient table or by constructing a dedicated breast imaging table, thereby allowing higher aspect ratio coils. In this design, the coil assembly would be constructed to allow positioning on either side of the table, depending on which breast was being imaged. A fiberglass or Kevlar sheath covering the coil assembly and running the length of the patient table would serve the dual functions of isolating the patient from the electrical and cooling circuits and providing an additional form of mechanical fixation to secure the coils on the table. Because the coils are not torque-balanced, it will be necessary to anchor the structure firmly, both from the point of view of vibration-induced imaging artifacts and of patient safety.

The high gradient efficiencies of these coils will allow much higher spatial-resolution imaging than can currently be achieved in a clinical setting, and additionally, will provide very large amplitude motion-sensitizing gradients, thus facilitating diffusion imaging (or flow imaging) in small blood vessels with short echo times. T_2 has been measured for human breast tissue, with reported values ranging between 60 and 150 ms (17, 18). Recently, we reported T_2 approximately 70 ms for human breast tumor (MCF7 human breast carcinoma) growing in a mouse mammary fat pad (19). More fibrous tumors can have significantly shorter T_2s. For this reason, initial signal loss at $b = 0$ s/mm^2 due to T_2 weighting of the image can severely limit the range of b factors for which images can be obtained, which has the result of limiting the precision of the ADC measurement. Our approach is to shorten TE while maintaining diffusion weighting by increasing diffusion gradient amplitudes. This gives a substantial increase in initial signal intensity for $b = 0$ s/mm^2, allowing high-quality images to be obtained for much higher b factors. Even in cases in which signal loss from T_2 weighting is not so severe as to limit ADC precision, the ability to obtain high diffusion weighting with short TE reduces dramatically the T_2 contrast in an image. This will allow acquisition of a diffusion-weighted image in which the contrast is determined mainly by tissue ADC rather than by a mix of ADC and T_2.

A secondary important benefit that can be gained using high-efficiency gradient coils is that the ramp time required to attain imaging gradient strengths (10–25 mT/m) is decreased from that required by whole-body coils by a factor of the efficiency (since the current slew rate is similar to whole-body coils, and the required peak current is decreased). This will enable echo-planar imaging (and other fast imaging techniques) using conventional gradient amplifiers. Echo-planar imaging techniques have been proven to be much less susceptible to motion artifacts than conventional imaging sequences (20) and have recently been applied to diffusion imaging *in vivo* (21) with good results.

For rapid imaging pulse sequences, and for high-amplitude bipolar pulses, very rapid changes in gradient polarity are required. Although the magnetic field amplitudes drop off quickly in the region above the coils, magnetic fields are also generated by the return wires on the horizontal plate, and excitation thresholds for cardiac stimulation must be considered. As an upper limit for one coil, $|B|$ was calculated for the G_z coil at various distances above the return wires at the location of the highest wire density. The maximum dI/dt from our gradient coil amplifiers is 200 A in 184 μs. This produces dB/dt = 156 T/s at 1 cm above the coil return wire plate

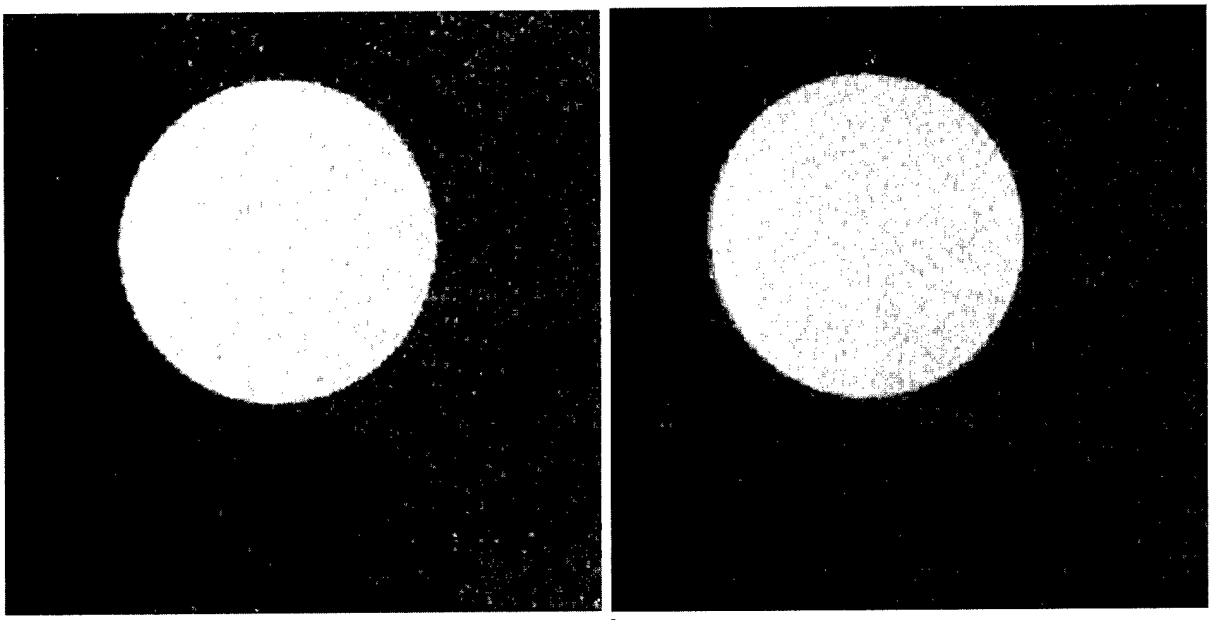

FIG. 9. ADC maps of a T_2 = 60 ms agar phantom obtained (a) using the whole-body coils to provide all diffusion and imaging gradients, TE = 80 ms, and (b) using the breast gradient coils to provide all gradients, where the diffusion gradient strengths were four times the whole-body gradient strengths and TE = 46 ms. In all cases, the ADC maps were constructed from 10 images with b = 0 to b = 1000 s/mm^2.

and dB/dt = 50 T/s at 10 cm, compared to a recommended upper limit of 400 T/s for cardiac stimulation (22). The magnitude of these fields is relatively small at regions of concern with respect to magnetic stimulation such as the heart; however, peripheral nerve stimulation has been reported at dB/dt as low as 40 T/s in some patients (22). Theoretical field calculations will allow prediction of $|B|$ and dB/dt for all pulse sequences before implementation, and pulse sequences will be tailored to adhere to maximum dB/dt and peak $|B|$ guidelines. Additionally, if peripheral nerve stimulation is reported for individual patients, dB/dt will be reduced below the stimulation threshold by increasing gradient switching times.

SUMMARY

We have constructed a three-axis gradient coil set for imaging human breast tumors. These coils create gradient efficiencies of up to 3.3 mT/m/A with relatively low inductance ($\leq$1000 μH), and good gradient uniformity over most of the volume required for breast imaging. Preliminary diffusion results were obtained in a water phantom for b factors as high as ~1000 s/mm^2 for TE = 46 ms. A compact, efficient water-cooling system was presented, which maintained coil temperatures at or below room temperature, even for RMS currents as high as 20 A. This gradient/cooling module will allow, for the first time, clinical breast imaging using diffusion and microvascular flow-weighted protocols with high spatial resolution.

REFERENCES

1. D. S. Webster, K. H. Marsden, Improved apparatus for the NMR measurement of self- diffusion coefficients using pulsed field gradients. *Rev. Sci. Instrum.* **45,** 1232–1234 (1974).
2. K. C. Chu, B. K. Rutt, Quadrupole gradient coil design and optimization: a printed circuit board approach. *Magn. Reson. Med.* **31,** 652–659 (1994).
3. W. G. O'Dell, J. S. Schoeniger, S. J. Blackband, E. R. McVeigh, A modified quadrupole gradient set for use in high resolution MRI tagging. *Magn. Reson. Med.* **32,** 246–250 (1994).
4. R. Turner, A target field approach to optimal coil design. *J. Phys. D. Appl. Phys.* **19,** L147–151 (1986).
5. R. Turner, Gradient coil design: a review of methods. *Magn. Reson. Med.* **11,** 903–920 (1993).
6. P. W. McOwan, T. W. Redpath, A specialised receiver coil for NMR imaging of female breasts. *Phys. Med. Biol.* **32,** 259–263 (1987).
7. J. P. Hornak, J. Szumowski, R. G. Bryant, Elementary single turn solenoids used as the transmitter and receiver in MRI. *Magn. Reson. Imaging* **5,** 233–237 (1987).
8. L. Sun, L. O. Olsen, P. L. Robitaille, Design and optimization of a breast coil for magnetic resonance imaging. *Magn. Reson. Imaging* **11,** 73–80 (1993).
9. E. O. Stejskal, J. E. Tanner, Spin diffusion measurements: spin echoes in the presence of a time-dependent field gradient. *J. Chem. Phys.* **42,** 288–292 (1965).
10. M. Neeman, J. P. Freyer, L. O. Sillerud, A simple method for obtaining cross-term-free images for diffusion anisotropy studies in NMR microimaging. *Magn. Reson. Med.* **21,** 138–143 (1991).
11. P. B. Roemer, Transverse gradient coils for imaging the head. United States Patent No. 5177442, January 5, 1993.
12. K. C. Chu, B. K. Rutt, MR gradient coil heat dissipation. *Magn. Reson. Med.* **34,** 125–132 (1995).
13. M. O'Donnell, W. A. Edelstein, NMR imaging in the presence of magnetic field inhomogeneities and gradient field nonlinearities. *Med. Phys.* **12,** 20–26 (1985).
14. A. Ersahin, H. K. Lee, O. Nalcioglu, Asymmetric gradient coil design for high resolution breast imaging, *in* "Proc., SMR and ESMRMB, 3rd

Annual Meeting, Nice, 1995," p. 954.
15. H. K. Lee, R. Raman, R. Slates, A. Ersahin, O. Nalcioglu, An optimized gradient coil for breast imaging, *in* "Proc., SMR and ESMRMB, 3rd Annual Meeting, Nice, 1995," p. 955.
16. B. A. Chronik, B. K. Rutt, Constrained length minimum inductance gradient coil design, *in* "Proc., ISMRM, 5th Annual Meeting, Vancouver, B.C., Canada, 1997," p. 53.
17. D. Z. J. Chu, W. S. Yamanashi, J. Frazer, C. F. Hazlewood, H. S. Gallager, A. W. Boddie, R. G. Martin, Proton NMR of human breast tumors: correlation with clinical prognostic parameters. *J. Surg. Oncol.* **36,** 1–4 (1987).
18. S. J. Graham, M. J. Bronskill, J. W. Byng, M. J. Yaffe, N. F. Boyd, Quantitative correlation of breast tissue parameters using MR and X-ray mammography. *Br. J. Cancer* **73,** 162–168 (1996).
19. C. F. Maier, Y. Paran, P. Bendel, B. K. Rutt, H. Degani, Quantitative diffusion imaging in implanted human breast tumors. *Magn. Reson. Med.* **37,** 576–581 (1997).
20. R. Turner, D. LeBihan, Single-shot diffusion imaging at 2.0 Tesla. *J. Magn. Reson.* **86,** 445–452 (1990).
21. R. Turner, D. LeBihan, A. S. Chesnick, Echo-planar imaging of diffusion and perfusion. *Magn. Reson. Med.* **19,** 247–253 (1991).
22. J. P. Reilly, Principles of nerve and heart excitation by time-varying magnetic fields, *in* "Biological effects and safety aspects of NMRI and spectroscopy." *Ann. N. Y. Acad. Sci.* **649,** 96–107 (1993).

Constrained Length Minimum Inductance Gradient Coil Design

Blaine A. Chronik, Brian K. Rutt

A gradient coil design algorithm capable of controlling the position of the homogeneous region of interest (ROI) with respect to the current-carrying wires is required for many advanced imaging and spectroscopy applications. A modified minimum inductance target field method that allows the placement of a set of constraints on the final current density is presented. This constrained current minimum inductance method is derived in the context of previous target field methods. Complete details are shown and all equations required for implementation of the algorithm are given. The method has been implemented on computer and applied to the design of both a 1:1 aspect ratio (length:diameter) central ROI and a 2:1 aspect ratio edge ROI gradient coil. The 1:1 design demonstrates that a general analytic method can be used to easily obtain very short gradient coil designs for use with specialized magnet systems. The edge gradient design demonstrates that designs that allow imaging of the neck region with a head-sized gradient coil can be obtained, as well as other applications requiring edge-of-cylinder regions of uniformity.

Key words: gradient coils; target field; current constraints; minimum inductance; constrained length.

INTRODUCTION

Advanced MR imaging and spectroscopy methods often require high performance gradient hardware, where performance is typically characterized by a combination of gradient efficiency (gradient strength per unit current) and switching speed. The design of gradient coils customized to a particular application is a method of realizing gains in both. One defining characteristic of customized gradient coils is that they conform closely to the anatomical region of interest and although this allows increased performance, subject access to the usable region of the coil becomes an important and nontrivial design consideration.

Gradient coil design methods can be divided into two general categories: "coil space" versus "reciprocal space" techniques. Coil space methods iteratively adjust the positions of wires on the gradient coil former until the design conforms to some desired performance specifications. The optimal wire configuration is chosen, using a numerical optimization technique, from the multitude of wire configurations that span the domain of allowable patterns. The method of Conjugate Gradient Descent (1, 2) and the method of Simulated Annealing (3–6) are examples of different optimization techniques applied to this problem. Although these methods in principle allow complete freedom in the wire pattern and can be applied to any geometry, they are in practice limited due to the computational intensity of the methods. They have been most effectively applied to the problem of positioning coaxial circular wire loops in the design of longitudinal (G_z) gradient coils; furthermore, when applied to the design of cylindrical transverse gradient coils (G_x or G_y), the functional form of the wire shapes have typically been predetermined to depend on only a few parameters so that the number of degrees of freedom remains practical. Advantages of these methods include the absence of an approximation stage in sampling a continuous current density with a finite number of wires, and most importantly the ease with which they incorporate direct constraints on the final wire pattern, thereby allowing the design of restricted length gradient coils. The first advantage is primarily of concern only when the current density is to be sampled with a small number of wires, since field variations due to finite wire spacing become insignificant at distances larger than that spacing.

Reciprocal space methods are characterized by the expansion of all quantities of interest in terms of orthogonal functions and solving for the coefficients of the corresponding current density expansion. The current density is then approximated by a finite set of wires, typically using stream function methods (7). Because of the difficulty in obtaining orthogonal function expansions for general geometries, in practice these techniques are limited to simple geometries (planes (8, 9), cylinders (10, 11), spheres (12), ellipses (13), hyperbolas (14)); furthermore, they often lack control over the final current density that is attainable with coil space methods (15). Once quantities of interest have been expanded and the coefficients of the current density expansion formally solved for, computer implementation of these methods is simple and current densities can be obtained very quickly. Reciprocal space methods can yield optimal designs by using constrained Lagrange multiplier or least squared error methods to solve for the expansion coefficients (16).

In this paper we address the problem of including direct control over current density in a reciprocal space design method. We present the details of a modification of Turner's minimum inductance target field method (17) that allows explicit constraint of the extent of the final current density as well as control over the position of the uniform gradient with respect to the current density while minimizing coil inductance. These modifications yield a design method with the generality claimed for

MRM 39:270–278 (1998)

From the Departments of Physics and Astronomy (B.A.C.) and Diagnostic Radiology and Nuclear Medicine (B.K.R.), University of Western Ontario, and Tom Lawson Family Imaging Research Laboratories (B.K.R.), John P. Robarts Research Institute, London, Ontario, Canada.

Address correspondence to: B. K. Rutt, Ph.D., Imaging Research Labs, Robarts Research Institute, London, Ontario, Canada N6A 5K8.

Received April 3, 1997; revised July 24, 1997; accepted July 24, 1997.

This work was supported by the Medical Research Council of Canada. B.A.C. is supported by an Natural Sciences and Engineering Research Council of Canada Postgraduate Scholarship.

0740-3194/98 $3.00

coil space methods and the efficiency of reciprocal space techniques.

THEORY

In any magnetic design problem the most important step is the establishment of a relationship between the current density function and the desired magnetic field components. For gradient coils used in MRI, we are only concerned with the z-component of the magnetic field, $B_z(r, \phi, z)$; furthermore, if we are considering axially aligned cylindrical gradient coils (define the coil axis to lie along the z direction), only the azimuthal component of current density, $J_\phi(\phi, z)$, contributes to $B_z(r, \phi, z)$ and therefore the problem reduces to obtaining the connection between these two quantities. There are several ways to express this relationship but one that has proved especially fruitful is the "target field" formalism first described by Turner (10). This formalism is characterized by the expansion of $B_z(r, \phi, z)$ in cylindrical harmonics (18):

$$B_z(r, \phi, z) = (-\mu_o a) \sum_{m=-\infty}^{\infty} \int_{-\infty}^{\infty} dk e^{im\phi} e^{i2\pi kz} |k| I_m(|2\pi kr|) K'_m(|2\pi ka|) j_\phi^m(k) \quad [1]$$

where I_m and K_m are modified Bessel functions, a is the radius of the cylinder on which the current is constrained to flow, and

$$j_\phi^m(k) = \int_{-\pi}^{+\pi} d\phi\, e^{-im\phi} \int_{-\infty}^{+\infty} dz\, e^{-i2\pi kz} J_\phi(\phi, z) \quad [2]$$

is the 2D Fourier Transform of $J_\phi(\phi, z)$ in cylindrical coordinates. All target field based methods express quantities of interest as functions of $j_\phi^m(k)$ and then directly solve for the $j_\phi^m(k)$ that yields the desired gradient coil. Methods only differ in terms of the physical quantities explicitly included in the design process and how the required $j_\phi^m(k)$ is solved for. It should be emphasized that all target field methods are direct inverse solutions to the gradient coil design problem and that once $j_\phi^m(k)$ is known, the current density obtained via inverse transformation of $j_\phi^m(k)$ will give the desired gradient coil, i.e., one which produces exactly the specified field.

"Original" Target Field

The original target field method developed by Turner (10) makes use of the fact that the 2D Fourier transform of $B_z(r, \phi, z)$ is very simply related to $j_\phi^m(k)$:

$$B_z^m(c, k) = \omega^m(c, k) j_\phi^m(k) \quad [3]$$

where

$$\omega^m(c, k) = (-\mu_o a)|k| I_m(|2\pi kc|) K'_m(|2\pi ka|) \quad [4]$$

and

$$B_z^m(c, k) = \int_{-\pi}^{+\pi} d\phi\, e^{-im\phi} \int_{-\infty}^{+\infty} dz\, e^{-i2\pi kz} B_z(c, \phi, z) \quad [5]$$

with c the radius of a cylindrical surface ($c < a$), called the "target cylinder." It is useful to think of $B_z^m(c, k)$ as an apodised version of $j_\phi^m(k)$, and $\omega^m(c, k)$ acting as the apodising function with limiting forms:

$$\omega^m(c, k) \sim e^{-2\pi k(a-c)}; \quad k \to \infty \quad [6a]$$

$$\omega^m(c, k = 0) = \frac{\mu_o c}{4\pi a} \quad [6b]$$

Knowing that $B_z^m(c, k)$ and $j_\phi^m(k)$ are related via a simple product translates into a convolution relationship between $B_z(c, \phi, z)$ and $J_\phi(\phi, z)$:

$$B_z(c, \phi, z) = \Omega(c, z) \otimes J_\phi(\phi, z) \quad [7]$$

where $\Omega(c, z)$ is the inverse transform of $\omega^m(c, k)$. $\Omega(c, z)$ is approximately Lorentzian in shape with full width at half-maximum proportional to (a-c); this means that the magnetic field has the same functional form as the azimuthal current density but "smeared" in the z direction by a Lorentzian-like function that gets broader as the target cylinder moves further away from the current-carrying cylinder. In other words, the longitudinal component of magnetic field is a "low-pass filtered" version of the azimuthal component of current density.

To obtain a gradient coil, the desired field on the target cylinder must be specified (i.e., the "target field"). Generally, we write:

$$B_z(c, \phi, z) = g(z) f(c, \phi) \quad [8]$$

where $g(z)$ is the field modulation along the z direction and $f(c, \phi)$ describes the radial and azimuthal variation of B_z. For longitudinal (G_z) gradient coils we would have $f(c, \phi)$ = constant and the regions of uniform gradient correspond to regions over which the first derivative of $g(z)$ is approximately constant. For transverse gradient coils (G_x or G_y) we would have:

$$f(c, \phi) = cG_x \cos\phi \quad [G_x] \quad [9a]$$

$$f(c, \phi) = cG_y \sin\phi \quad [G_y] \quad [9b]$$

and regions of uniform gradient correspond to regions over which $g(z)$ is approximately constant.

Taking a G_x coil as an example, we combine Eqs. [8] and [9a], substitute the resulting expression for $B_z^m(c, k)$ into Eq. [3] and solve for $j_\phi^m(k)$ to get:

$$j_\phi^l(k) = \frac{cG_x\pi \cdot \Im\{g(z)\}}{\omega^l(c, k)} \quad [10a]$$

$$j_\phi^m(k) = 0; \quad \text{for} \quad m \neq 1 \quad [10b]$$

where $\Im\{g(z)\}$ is the 1D Fourier transform of $g(z)$. Once $g(z)$ has been specified over all z points, the $j_\phi^l(k)$ func-

tion is easily arrived at using Eq. [10a] and $J_\phi(\phi, z)$ obtained by inverse transformation. The $J_z(\phi, z)$ current density component is obtained from $J_\phi(\phi, z)$ by imposing continuity of $\vec{J}(\phi, z)$ (7, 19). It should be noted that although the forms in this paper are general in that they include the complete range of possible m values, the expressions applied to longitudinal and transverse gradient coils greatly simplify to include only the $m = 0$ and $m = \pm 1$ contributions respectively.

Minimum Inductance Target Field

The minimum inductance target field method represents a rather different and more powerful way of solving for $j_\phi^m(k)$ in that we now determine the $j_\phi^m(k)$ that minimizes some property of the gradient coil (typically inductance or power dissipation) subject to the constraint that B_z be equal to specified values (B_{zn}) at a finite set of coordinates (r_n, ϕ_n, z_n). The result of the analysis is still $j_\phi^m(k)$ (the transform of which gives the required current density) and Eq. [3] still holds; however, $j_\phi^m(k)$ is solved for differently.

To set a context for the extension described in this paper, we review the form of the minimum inductance method, first described by Turner (17). It is an application of the method of constrained optimization using Lagrange multipliers (19). A functional, $U\{j_\phi^m(k)\}$, is formed that includes the function, $F\{j_\phi^m(k)\}$ to be optimized (typically F is either inductance, L, or power dissipation, P, both of which are expressible as functions of the current density) and the field constraint equations multiplied by constants, λ_n, the Lagrange multipliers:

$$U\{j_\phi^m(k)\} = F\{j_\phi^m(k)\} + \sum_n \lambda_n[B_z(r_n, \phi_n, z_n) - B_{zn}] \qquad [11]$$

In a manner analogous to the optimization of a function of a single variable, the derivative of U with respect to $j_\phi^m(k)$ is taken and set equal to zero. We then solve that equation for $j_\phi^m(k)$. For the specific case of minimizing coil inductance, we first write L as a function of $j_\phi^m(k)$ (17, 20):

$$L = \left(\frac{-\mu_o a^2}{2\pi I^2}\right) \sum_{m=-\infty}^{+\infty} \int_{-\infty}^{+\infty} \cdot dk \qquad [12]$$
$$I'_m(|2\pi ka|)\, K'_m(|2\pi ka|) j_\phi^m(k)^2$$

where I is the input current required to produce the surface current density, then note the form of the field constraint equations:

$$B_z(r_n, \phi_n, z_n) - B_{zn} = 0 \qquad [13a]$$

$$\left[(-\mu_o a) \sum_{m=-\infty}^{+\infty} \int_{-\infty}^{+\infty} dk e^{im\phi_n} e^{i2\pi k z_n |k|}\right. \qquad [13b]$$
$$\left. I_m(|2\pi kr_n|)\, K'_m(|2\pi ka|) j_\phi^m(k)\right] - B_{zn} = 0$$

Differentiating U composed of Eqs. [12] and [13b] and solving for $j_\phi^m(k)$ yields:

$$j_\phi^m(k) = \sum_{n=1}^{N} \lambda_n a_n^m(k) \qquad [14]$$

$$a_n^m(k) = \left(\frac{-\pi}{a}\right) e^{im\phi_n} e^{i2\pi k z_n |k|} \frac{I_m(|2\pi kr_n|)}{I'_m(|2\pi ka|)} \qquad [15]$$

Once the set of λ_n is known, Eqs. [14] and [15] give the required $j_\phi^m(k)$. The λ_n's are determined by substituting $j_\phi^m(k)$ as expressed by Eq. [14] into the N constraint equations of Eq. [13b]. This can be written as a matrix equation for the λ_n's:

$$[\mathbf{M_{11}}][\lambda_N] = [\mathbf{B}_{zN}] \qquad [16]$$

where the elements of matrix $\mathbf{M_{11}}$ are known functions of the constraint coordinates and are given as the first row of Table 1. The design algorithm is then simply to choose the N field constraints, calculate the elements of $\mathbf{M_{11}}$ from the constraint coordinates and the equations shown in Table 1, solve Eq. [16] for the set of $\{\lambda_n\}$, compose $j_\phi^m(k)$ via Eq. [14] and inverse transform to get $J_\phi(\phi, z)$.

Constrained Current Minimum Inductance Target Field

To add explicit control over the length (and boundaries) of the final current density to the design algorithm, we have modified Turner's minimum inductance method to include a set of current constraints. This type of control over the design is very important when the region of good uniformity is required to be near the extremes of the physical coil, as well as when the total gradient coil length needs to be minimized.

The first form of current constraint that one would want to impose upon a design is a "closure" constraint that prevents any current density from crossing the boundaries of a specified area on the surface of the cylindrical former. This constraint manifests itself in the final coil design as forcing all conducting loops within the specified region to be closed. A simple form of this constraint would be to require that no current density cross the azimuthal lines defined by $\pm z_q$. Analytically this is equivalent to requiring that the integral of $J_\phi(\phi, z)$ on the line along any $\phi = \phi_q$ from $-z_q$ to $+z_q$ be zero:

$$\Lambda(\phi_q, z_q) = \int_{-z_q}^{+z_q} J_\phi(\phi_q, z) dz = 0 \qquad [17]$$

For longitudinal gradient coils this constraint does not need to be applied because the z component of current density will always be zero. For transverse gradient coils the azimuthal variation of $J_\phi(\phi, z)$ is always sinusoidal; therefore, the integral constraint only needs to be applied over a single line from $-z_q$ to $+z_q$ (i.e., along constant $\phi = \phi_q$).

The second type of current constraints necessary to force the current density to remain contained within some region of the coil surface are direct constraints on

Table 1
Analytic Forms for the Calculation of Matrix Elements and Subsequent Determination of Lagrange Multipliers in the Constrained Current Minimum Inductance Design Method

$$M_{11}(n, n') = \sum_{m=-\infty}^{+\infty} \int_{-\infty}^{+\infty} dk \Psi_n^m(k) a_{n'}^m(k) = (\pi \mu_o I) \sum_{m=-\infty}^{+\infty} \int_{-\infty}^{+\infty} dk e^{im(\phi_n + \phi_{n'})} e^{i2\pi k(z_n + z_{n'})} |k|^2 \frac{K'_m(|2\pi ka|)}{I'_m(|2\pi ka|)} I_m(|2\pi kr_n|) I_m(|2\pi kr_{n'}|) w^2(k)$$

$$M_{12}(n, p') = \sum_{m=-\infty}^{+\infty} \int_{-\infty}^{+\infty} dk \Psi_n^m(k) b_{p'}^m(k) = \left(-\frac{\pi I}{a} \right) \sum_{m=-\infty}^{+\infty} \int_{-\infty}^{+\infty} dk e^{im(\phi_n + \phi_{p'})} e^{i2\pi k(z_n + z_{p'})} |k| \frac{I_m(|2\pi kr_n|)}{I'_m(|2\pi ka|)} w^2(k)$$

$$M_{13}(n, q') = \sum_{m=-\infty}^{+\infty} \int_{-\infty}^{+\infty} dk \Psi_n^m(k) c_{q'}^m(k) = \left(-\frac{2\pi I}{a} z_{q'} \right) \sum_{m=-\infty}^{+\infty} \int_{-\infty}^{+\infty} dk e^{im(\phi_n + \phi_{q'})} e^{i2\pi kz_n} |k| \mathrm{sinc}(2\pi kz_{q'}) \frac{I_m(|2\pi kr_n|)}{I'_m(|2\pi ka|)} w^2(k)$$

$$M_{22}(p, p') = \sum_{m=-\infty}^{+\infty} \int_{-\infty}^{+\infty} dk \Phi_p^m(k) b_{p'}^m(k) = \left(\frac{\pi I}{\mu_o a^2} \right) \sum_{m=-\infty}^{+\infty} \int_{-\infty}^{+\infty} dk e^{im(\phi_p + \phi_{p'})} e^{i2\pi k(z_p + z_{p'})} \frac{w^2(k)}{I'_m(|2\pi ka|) K'_m(|2\pi ka|)}$$

$$M_{23}(p, q') = \sum_{m=-\infty}^{+\infty} \int_{-\infty}^{+\infty} dk \Phi_n^m(k) c_{q'}^m(k) = \left(\frac{2\pi I}{\mu_o a^2} z_{q'} \right) \sum_{m=-\infty}^{+\infty} \int_{-\infty}^{+\infty} dk e^{im(\phi_p + \phi_{q'})} e^{i2\pi kz_p} \mathrm{sinc}(2\pi kz_{q'}) \frac{w^2(k)}{I'_m(|2\pi ka|) K'_m(|2\pi ka|)}$$

$$M_{33}(q, q') = \sum_{m=-\infty}^{+\infty} \int_{-\infty}^{+\infty} dk \Gamma_q^m(k) c_{q'}^m(k) = \left(\frac{4\pi I}{\mu_o a^2} z_q^2 \right) \sum_{m=-\infty}^{+\infty} \int_{-\infty}^{+\infty} dk e^{im(\phi_q + \phi_{q'})} \mathrm{sinc}^2(2\pi kz_q) \frac{w^2(k)}{I'_m(|2\pi ka|) K'_m(|2\pi ka|)}$$

the values of the azimuthal current density over a set of coordinates:

$$J_\phi(\phi_p, z_p) = J_{\phi p}; \quad p = 1{:}P \qquad [18]$$

Azimuthal current constraints of this form have been introduced previously (21); however, it should be noted that only the use of both the above forms of current constraint (closure and point azimuthal constraints) provides a sufficient and necessary condition for current density to be zero beyond $\pm z_{q'}$. The closure constraint alone does not disallow closed current loops outside the bounded region whereas constraining the azimuthal current density to be zero does not prohibit non-zero longitudinal current density, $J_z(\phi, z)$ at the P constraint points; this will be made clear by example in the Results section.

Mathematically the current constraints represent a simple extension of the minimum inductance method outlined above. Both the closure constraint and the P current constraints must first be expressed as functions of $j_\phi^m(k)$:

$$\Lambda(\phi_q, z_q) = (2z_q) \sum_{m=-\infty}^{+\infty} \int_{-\infty}^{+\infty} dk e^{im\phi_q} \mathrm{sinc}(2\pi kz_q) j_\phi^m(k) \qquad [19a]$$

$$J_\phi(\phi_p, z_p) = \sum_{m=-\infty}^{+\infty} \int_{-\infty}^{+\infty} dk e^{im\phi_p} e^{i2\pi kz_p} j_\phi^m(k) \qquad [19b]$$

With the constraint equations written as above, the functional to be optimized would take a form similar to Eq. [11] and the optimal $j_\phi^m(k)$ obtained as before; however, there is a practical issue involved in the constraint of current that gives reason to alter Eq. [19]. The prescription of $J_\phi(\phi, z)$ at a finite set of points does not prevent large values of $J_\phi(\phi, z)$ between the constraint points. As the current constraints are moved closer together (requiring a larger number of constraints to cover the same area) non-zero interconstraint $J_\phi(\phi, z)$ values correspond to increasing power at high spatial frequencies, i.e., at high k values in $j_\phi^m(k)$. Although there is no theoretical limitation on the spatial frequency content of $J_\phi(\phi, z)$, any practical design will involve a maximum tolerable spatial frequency. The particular frequency will depend on the application and will often be determined by both the width and minimum bending radius of the conductor to be used in the final winding of the coil. For these reasons we filter out the impractically high frequency components of $J_\phi(\phi, z)$ via an apodizing function $w(k)$:

$$J_\phi(\phi, z) = \sum_{m=-\infty}^{+\infty} \int_{-\infty}^{+\infty} dk e^{im\phi} e^{i2\pi kz} w(k) j_\phi^m(k) \qquad [20]$$

where in the present work, we have used the following functional form for $w(k)$:

$$w(k) = 1, \quad |k| < k_t$$

$$= \frac{1}{2}\left[1 + \cos\left(\pi \cdot \frac{|k| - k_t}{k_c - k_t} \right) \right], \quad k_t \le |k| < k_c \qquad [21]$$

$$= 0, \quad |k| \ge k_c$$

with k_t ("transition frequency") and k_c ("cutoff frequency") chosen based on the desired complexity of the final current density. To prevent changes in the direction of $J_\phi(\phi, z)$ from occurring on a scale smaller than Δz (for example, Δz could be set equal to twice the minimum turning radius of the wire to be used in coil construction), k_c should be set equal to $1/(2*\Delta z)$; k_t is then set to allow a smooth transition in $w(k)$ while preventing the attenuation of frequency components below k_t. It should be noted that the spacing of the current constraints is set equal to $1/(2*k_c)$ to prevent nonzero values of current density between constraint positions. Examples of specific transition and cutoff frequency values used in practical designs will be given in the Results section. We now apply the closure and current constraints to $J_\phi(\phi, z)$ given above:

$$\Lambda(\phi_q, z_q) = \sum_{m=-\infty}^{+\infty} \int_{-\infty}^{+\infty} dk \Gamma_q^m(k) j_\phi^m(k) \qquad [22]$$

$$\Gamma_q^m(k) = (2z_q) e^{im\phi_q} \mathrm{sinc}(2\pi k z_q) w(k) \qquad [23]$$

and

$$J_\phi(\phi_p, z_p) = \sum_{m=-\infty}^{+\infty} \int_{-\infty}^{+\infty} dk \Phi_p^m(k) j_\phi^m(k) \qquad [24]$$

$$\Phi_p^m(k) = e^{im\phi_p} e^{i2\pi k z_p} w(k) \qquad [25]$$

The apodizing function $w(k)$ must also be incorporated into the B_z constraint expressions to assure that the field constraints will be met by the constructed current density:

$$B_z(r_n, \phi_n, z_n) = \sum_{m=-\infty}^{+\infty} \int_{-\infty}^{+\infty} dk \Psi_n^m(k) j_\phi^m(k) \qquad [26]$$

$$\Psi_n^m(k) = (-\mu_o a) e^{im\phi_n} e^{i2\pi k z_n} |k| I_m(|2\pi k r_n|) \cdot K'_m(|2\pi k a|) w(k) \qquad [27]$$

Only the three sets of constraint equations are modified with the inclusion of $w(k)$; the inductance expression of Eq. [12] does not require apodization. The integrand of Eq. [12] naturally attenuates high spatial frequencies more extremely than $w(k)$ and therefore its inclusion is unnecessary. The attenuating property of the inductance integrand can be seen by noting that for large k, $I_m(k) \sim e^k/(\sqrt{2\pi k})$, $K_m(k) \sim e^{-k}/(\sqrt{2\pi k})$, and therefore the product is approximately $1/k$.

With the apodization discussed above, the functional to be minimized takes the form:

$$U\{j_\phi^m(k)\} = L\{j_\phi^m(k)\} + \sum_{n=1}^{N} \lambda_n [B_z(r_n, \phi_n, z_n) - B_{zn}] + \sum_{p=1}^{P} \lambda_p [J_\phi(\phi_p, z_p) - J_{\phi p}] + \lambda_q [\Lambda(\phi_q, z_q) - \Lambda_q] \qquad [28]$$

where the inductance expression is given by Eq. [12] and the summation over all constraints is that of Eq. [11] with $N+P+1$ constraints based on Eqs. [22], [24], and [26]. Taking the derivative of $U\{j_\phi^m(k)\}$ with respect to $j_\phi^m(k)$, setting the result equal to zero, and solving for $j_\phi^m(k)$, we get:

$$j_\phi^m(k) = \sum_{n=1}^{N} \lambda_n a_n^m(k) + \sum_{p=1}^{P} \lambda_p b_p^m(k) + \lambda_q c_q^m(k) \qquad [29]$$

where

$$a_n^m(k) = \left(\frac{-\pi}{a}\right) e^{im\phi_n} e^{i2\pi k z_n} |k| \frac{I_m(|2\pi k r_n|)}{I'_m(|2\pi k a|)} w(k) \qquad [30]$$

$$b_p^m(k) = \left(\frac{\pi}{\mu_o a^2}\right) e^{im\phi_p} e^{i2\pi k z_p} \frac{w(k)}{I'_m(|2\pi k a|) K'_m(|2\pi k a|)} \qquad [31]$$

$$c_q^m(k) = \left(\frac{2\pi z_q}{\mu_o a^2}\right) e^{im\phi_q} \mathrm{sinc}(2\pi k z_q) \cdot \frac{w(k)}{I'_m(|2\pi k a|) K'_m(|2\pi k a|)} \qquad [32]$$

The set of $\{\lambda_n, \lambda_p, \lambda_q\}$ (representing $N+P+1$ total unknowns) is found by substituting $j_\phi^m(k)$ expressed by Eq. [29] into the $N+P+1$ constraint Eqs. [22], [24], and [26] to get the following:

$$B_{zn} = \sum_{m=-\infty}^{+\infty} \int_{-\infty}^{+\infty} dk \Psi_n^m(k) \left[\sum_{n'=1}^{N} \lambda_{n'} a_{n'}^m(k) + \sum_{p'=1}^{P} \lambda_{p'} b_{p'}^m(k) + \lambda_{q'} c_{q'}^m(k) \right] \qquad [33]$$

$$J_{\phi p} = \sum_{m=-\infty}^{+\infty} \int_{-\infty}^{+\infty} dk \Phi_p^m(k) \left[\sum_{n'=1}^{N} \lambda_{n'} a_{n'}^m(k) + \sum_{p'=1}^{P} \lambda_{p'} b_{p'}^m(k) + \lambda_{q'} c_{q'}^m(k) \right] \qquad [34]$$

$$\Lambda_q = \sum_{m=-\infty}^{+\infty} \int_{-\infty}^{+\infty} dk \Gamma_q^m(k) \left[\sum_{n'=1}^{N} \lambda_{n'} a_{n'}^m(k) + \sum_{p'=1}^{P} \lambda_{p'} b_{p'}^m(k) + \lambda_{q'} c_{q'}^m(k) \right] \qquad [35]$$

This set of equations can be written as a single matrix equation, the solution of which is a vector of the required Lagrange multipliers:

$$\mathbf{M}\boldsymbol{\lambda} = \mathbf{c} \qquad [36]$$

In block form Eq. [36] is:

$$\begin{bmatrix} \mathbf{M}_{11} & \mathbf{M}_{12} & \mathbf{M}_{13} \\ \mathbf{M}_{12}^{T} & \mathbf{M}_{22} & \mathbf{M}_{23} \\ \mathbf{M}_{13}^{T} & \mathbf{M}_{23}^{T} & \mathbf{M}_{33} \end{bmatrix} \begin{bmatrix} \boldsymbol{\lambda}_{N} \\ \boldsymbol{\lambda}_{P} \\ \boldsymbol{\lambda}_{Q} \end{bmatrix} = \begin{bmatrix} \mathbf{B}_{zN} \\ \mathbf{J}_{\phi P} \\ \boldsymbol{\Lambda}_{Q} \end{bmatrix} \qquad [37]$$

where the six distinct blocks of the matrix are all known functions of the constraint coordinates and are listed in Table 1. The $\mathbf{M_{11}}$ block is identical to that used in Eq. [16] but derived using $a_n^m(k)$ given by Eq. [30] instead of Eq. [15], and the elements are functions of the field constraint coordinates only. If the azimuthal current constraints are included, the resulting $N+P$ by $N+P$ matrix is composed of $\mathbf{M_{11}}$, $\mathbf{M_{12}}$, and $\mathbf{M_{22}}$; here $\mathbf{M_{22}}$ is only a function of the current constraint coordinates whereas $\mathbf{M_{12}}$ is a function of both the field and current coordinates. The inclusion of the closure constraint increases the dimension of the matrix by 1 (now of rank $N+P+1$) and $\mathbf{M_{33}}$ depends only on the closure coordinates. The $\mathbf{M_{23}}$ block includes both closure and current coordinates while $\mathbf{M_{13}}$ has both closure and field coordinates. The Lagrange multiplier vector would be $\{\lambda_n\}$ for only field constraints, $\{\lambda_n, \lambda_p\}$ for field and current, $\{\lambda_n, \lambda_q\}$ for field and closure, and $\{\lambda_n, \lambda_p, \lambda_q\}$ for all three types of constraints. The constant vector on the right hand side of Eq. [37] is partitioned in an analogous way.

With the above mathematical forms in place, the design algorithm is simply the following. First a set of constraints is chosen that will assure that the gradient coil will fall within specifications. The field constraints determine the type of gradient coil (transverse versus longitudinal), the gradient strength, and the size and absolute placement of the region of uniformity. Current and closure constraints are chosen such that the physical coil will be of the required size and the region of gradient uniformity is positioned as desired relative to the current density. Once all constraints are set, the elements of matrix $\mathbf{M}$ are computed via the known forms in Table 1 and the constraint vector is assembled. Equation [37] is solved for the Lagrange multipliers through Gaussian elimination or an alternative technique. The multipliers are used in Eq. [29] to yield $j_\phi^m(k)$, the transform of which gives the current density of minimum inductance satisfying all of the specified design constraints.

RESULTS AND DISCUSSION

The theory in the previous section has been implemented in the MATLAB software language (version 4.2, The Mathworks Inc., Natick, MA) and used to create a variety of gradient coil designs, representative examples of which are presented in the following paragraphs. The azimuthal current density, $J_\phi(\phi, z)$, is the final result of the above analysis; however, the discrete wire pattern approximating the current density is obtained via stream function methods described elsewhere (7). The entire calculation, from specification of all constraints to determination of $J_\phi(\phi, z)$ and the approximation with discrete wire paths, typically takes less than three minutes on a Sun Microsystems ULTRA SPARC 1/140 workstation. All analytic forms involved in the evaluation of the matrix elements of Table 1 and subsequent construction of $J_\phi(\phi, z)$ are well known (exponential and modified Bessel functions) and there are readily available and accurate routines within the MATLAB package for their evaluation. Once the final wire pattern is obtained, the pattern for the entire coil is discretized into on the order of 10,000 to 20,000 elements, allowing for numerical verification of the achieved magnetic fields and inductance using the Biot-Savart equation and Neumann's formula (22), respectively. Gradient efficiency (η, defined as gradient strength per unit current) can be gained at the cost of increasing coil inductance simply by increasing the number of wires used to sample the current density. Efficiency varies linearly with wire number while the inductance increases as the square of the wire number. Inductance also varies as the fifth power of coil radius (for constant efficiency and wire pattern (16)); therefore, for a given design, $\eta \cdot a^{2.5}/(\sqrt{L})$ is a constant, independent of both radius and wire number. We use this quantity as a figure-of-merit or performance measure in comparing different designs.

The most familiar gradient coil application is the establishment of a uniform gradient field within the central region of a current carrying cylinder. To demonstrate the effectiveness of the combination of closure and current constraints in limiting the extent of the final current density, the four different combinations of constraints described in the theory section: field, field and closure, field and current, and field, closure, and current, were applied to the problem of designing an extremely short aspect ratio (1:1, coil length:coil diameter) central region of interest (ROI) coil. Field constraints must always be included because the minimum inductance current density not constrained to produce any field is simply zero everywhere. It has been suggested in the literature (5) that such extremely short coil designs are not possible with target field methods; this example serves to demonstrate that using the methods developed in this paper, very short aspect ratio coils can be designed in a straightforward manner. An ROI of length $0.75*a$ was chosen over which four field constraints were placed: $r_n = a/4$, $\phi_n = 0$, $z_n = \{-3, -1, 1, 3\}*(a/8)$ with $B_{zn} = G_x*r_n$ where G_x is the transverse gradient strength in T/m. The design corresponding to those specifications is shown in Figs. 1a and 1b. The coil has an aspect ratio of over 2.5:1 with the edge of the ROI located more than $2a$ away from the edge of the coil. To limit the aspect ratio to 1:1 while maintaining the size of the central ROI, a closure constraint was placed at the desired position (z_q) and a series of current constraints placed over the adjacent region; specifically, the closure constraint was $\Lambda = 0$ for $\phi_q = 0$, $z_q = a$ and the current constraints were $J_{\phi p} = 0$ at $\phi_p = 0$, $z_p = \pm\{(z_q + dz*i)$; for $i = 0{:}55$ and $dz = (3a/55)\}$. The apodization function, $w(k)$, was of the form given in Eq. [21] with $k_c = 1/(2*dz)$ and $k_t = 0.6*k_c$, set to prevent non-zero $J_\phi(\phi, z)$ between constraint points. This constitutes 117 constraints in total ($N = 4$, $P = 2*56 = 112$, $Q = 1$) and the results are shown in Figs. 1c–1h. The effects of the closure and current constraints applied separately are shown in Figs. 1c–1d and 1e–1f, respectively. Figures 1c–1h demonstrate that the combination of closure and current constraints is a sufficient condition for the con-

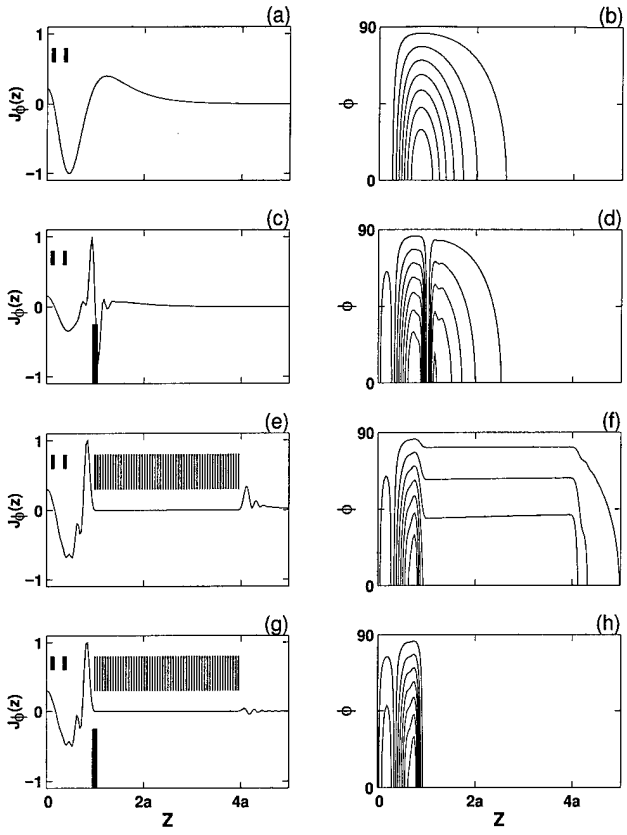

FIG. 1. Middle ROI, normalized $J_\phi(z)$s with corresponding half-quadrant wire paths for: (a–b) field constraints only (short heavy bars); (c–d) field and closure (long heavy bar) constraints; (e–f) field and current (long bars); (g–h) field, current, and closure constraints. All constraints are placed symmetrically about z = 0.

straint of gradient coil length and they must be used together to be effective in that regard. The calculated gradient efficiencies and inductances for the respective designs are shown in Table 2 for $a = 0.325$ m (approximate radius for a full body gradient coil). As expected, the merit figure and the aspect ratio decrease as constraints are added; however, access to the usable region is significantly improved. For the 1:1 design, the region of 20% gradient deviation extends over a cylinder of diameter 0.20 m and length 0.30 m at the coil center, beginning 0.20 m from the coil edge, whereas for the 2.5:1 design, the same region extends over a cylinder of diameter 0.30 m and length 0.40 m at the coil center, beginning 0.75 m from the coil edge. Figure 2a shows calculated contours of 20% gradient deviation on the *xz* plane for both the 2.5:1 and 1:1 aspect ratio designs. It can be seen that the uniformity of the gradient field is not compromised in a major way through the addition of the current constraints. The wire pattern for the 1:1 design is only slightly more complex than the 2.5:1 design, the only potential concern is the increased current density at the coil edge. This increased density is common to constrained length gradient coil designs, and is typically only two to three times the maximum density of the pure minimum inductance designs. Increasing the aspect ratio results in a decreased current density at the coil edge and the two can be traded off against each other in a controlled manner.

Table 2
Gradient Design Example Results Summary

	Coil Parameters		
	Efficiency [mT/m/A]	Inductance [μH]	Merit [*10^{-5}][a]
Central ROI designs[b]			
Field constraints	0.090	540	28
Field + closure constraints	0.074	604	22
Field + current constraints	0.070	656	20
Field + closure + current	0.055	690	15
Edge ROI designs[b]			
Field constraints	0.061	465	17
Field + closure constraints	0.057	460	16
Field + current constraints	0.053	520	14
Field + closure + current	0.032	290	11

[a] Merit = $(\eta * a^{2.5})/L^{1/2}$ in S.I. units.
[b] Both design sets are for $a = 0.325$ m.

As the above example suggests, the ability to restrict current density to a specified region of the coil allows for the control of the position of the ROI with respect to the physical end of the coil; an important extension of this idea is the design of gradient coils with a usable region of uniformity arbitrarily close to the end of the coil. To design such an edge gradient coil, a set of field constraints was placed over the edge ROI just as was done in the design described above. A second set of field constraints was placed at the opposite end of the coil, forcing the first moment of the current density to be zero by symmetry, thereby guaranteeing a torque balanced coil

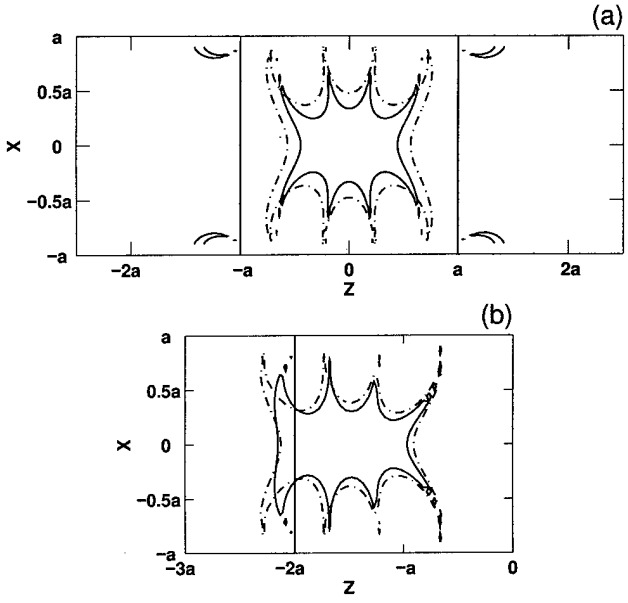

FIG. 2. Contour plots of 20% deviation from uniformity over *xz* planes for designs with and without current constraints. (a) shows 20% contours for the central ROI designs with (solid line) and without (dotted line) current constraints. The solid vertical line indicates the physical edge of the coil for the 1:1 aspect ratio design. (b) shows 20% contours over one half of the *xz* plane for the edge ROI designs with (solid line) and without (dotted line) current constraints. The vertical line indicates the position of the physical edge of the coil for the current constrained design.

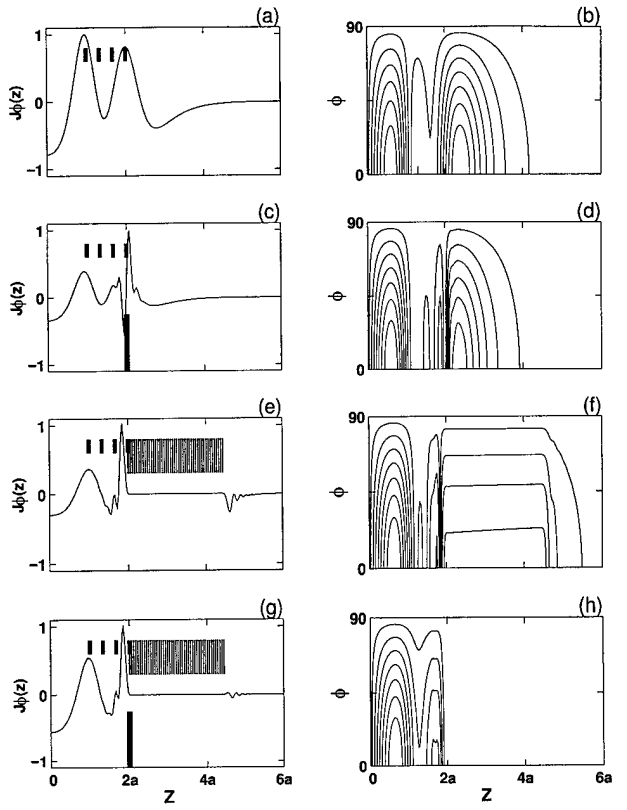

FIG. 3. Edge ROI, normalized $J_\phi(z)$s with corresponding half-quadrant wire paths for: (a–b) field constraints only (short heavy bars); (c–d) field and closure (long heavy bar) constraints; (e–f) field and current (long bars); (g–h) field, current, and closure constraints. All constraints are placed symmetrically about z = 0. Note relative position of closure, current, and field constraints yielding the edge gradient coil.

(20). No field constraints were specified over the central region because that area will not be utilized and unnecessary constraints only serve to increase the inductance of the design. The end of the coil was moved adjacent to the ROI by applying closure at the outer edges of the field constraint sets and a set of current constraints applied over the region exterior to the closure positions. As an example, four field constraints were placed over a region extending from $z = a$ to $z = 2a$: $r_n = a/4$, $\phi_n = 0$, $z_n = \{a + (a/3)*i\}$, where $i = 0{:}3$ with $B_{zn} = G_x \cdot r_n$. The same set was placed over the corresponding region on the negative side of the coil, constituting eight field constraints in total. The minimum inductance design subject to these field constraints is shown in Figs. 3a and 3b. The aspect ratio of the design is more than 4:1 and the outer edge of the ROI is more than $2a$ away from the edge of the coil. The addition of the closure constraint at $\phi_q = 0$, $z_q = \max(z_n) = 2a$, and the set of current constraints: $J_{\phi p} = 0$ at $\phi_p = 0$, $z_p = \pm\{(z_q + dz*i)$; for $i = 0{:}45$ and $dz = (2a/45)\}$, constitutes 101 constraints in total ($N = 8$, $P = 2*46 = 92$, $Q = 1$) and as in the central ROI design example, $w(k)$ was as shown in Eq. [21] with $k_c = 1/(2*dz)$ and $k_t = 0.6*k_c$; this results in the edge gradient coil design shown in Figs. 3g and 3h. For $a = 0.325$ m (approximate body coil dimension) the region of 20% gradient uniformity begins 7 cm *outside* the edge of the coil and ends 32 cm inside. For comparison, Figs. 3c–3f show the results of applying the closure and current constraints separately. The calculated gradient efficiencies and inductances are listed in Table 2. Figure 2b shows the calculated contours of 20% gradient deviation on the *xz* plane for designs with and without the above current constraints; again, it can be seen that the current constraints do not significantly affect the achieved gradient homogeneity. The edge coil wire pattern is not significantly more complicated than the unconstrained version of Fig. 3b nor is the maximum current density (located at the end of the coil) extreme, being slightly more than twice its maximum value in the unconstrained example. Just as in the 1:1 central ROI design example, the positioning of the ROI at the coil edge is accompanied by a decrease in the merit figure. The achieved merit figure depends on the size and position of the specified ROI with respect to the allowed extent of the current density. These can be traded off against each other for any particular application.

The ability to constrain the position of the imaging region with respect to the physical gradient coil with target field methods should represent an important improvement in gradient coil design in general. The minimum inductance target field method already developed possesses the advantage that it is an inverse solution to the design problem. It is a very numerically efficient technique that takes advantage of the FFT algorithm (23) and its use allows the designer to gain an understanding of the connection between spatial frequency components of the magnetic field and current density. We believe that one of the major limitations of target field methods has been the lack of direct control over the nature of the final form of the current density. The theory described in this paper removes this limitation. There are several important applications of this method. The constraint of total coil length for a middle ROI coil will allow the optimal design of gradients for use with short-bore magnets. It is also useful to limit gradient coil lengths simply for ease of construction and potential reduction of associated costs. Head sized gradient coil design will especially benefit from this method. The positioning of the ROI directly adjacent to the coil edge will allow, for the first time, imaging of the neck region with a head-sized gradient coil. It should also allow the imaging of the brain region with the subject's eyes positioned at or outside the coil edge. This would be useful in functional imaging studies where visual communication with the subject is necessary. We have designed a head-sized gradient coil capable of imaging with efficiencies of 0.4 mT/m/A over a region adjacent to the coil edge and having an inductance of 800 μH; we will report on the details of this design and experimental results of imaging with this coil in a forthcoming paper. The ability to easily design gradients of this nature should make possible new imaging methods that were previously considered impractical.

REFERENCES

1. E. Wong, A. Jesmanowicz, J. S. Hyde, Coil optimization for MRI by conjugate gradient descent. *Magn. Reson. Med.* **21**, 39–48 (1991).
2. E. R. Andrew, E. Szczesniak, Low inductance transverse gradient

system of restricted length. *Magn. Reson. Imaging* **13,** 607–613 (1995).
3. S. Crozier, D. M. Doddrell, Gradient-coil design by simulated annealing. *J. Magn. Reson.* **103,** 354–357 (1993).
4. S. Crozier, L. K. Forbes, D. M. Doddrell, The design of transverse gradient coils of restricted length by simulated annealing. *J. Magn. Reson. A.* **107,** 126–128 (1994).
5. S. Crozier, D. M. Doddrell, A design methodology for short, whole-body, shielded gradient coils for MRI. *Magn. Reson. Imaging* **13,** 615–620 (1995).
6. M. L. Buszko, M. F. Kempka, E. Szczesniak, D. C. Wang, E. R. Andrew, Optimization of transverse gradient coils with coaxial return paths by simulated annealing. *J. Magn. Reson. B.* **112,** 207–213 (1996).
7. W. A. Edelstein, J. F. Schenck, Current streamline method for coil construction. US Patent 4,840,700; priority date July 13, 1987.
8. K. Yoda, Analytic design method of self-shielded planar coils. *J. Appl. Phys.* **67,** 4349–4353 (1990).
9. M. A. Martens, L. S. Petropoulos, R. W. Brown, J. H. Andrews, M. A. Morich, J. L. Patrick, Insertable biplanar gradient coil for MR imaging. *Rev. Sci. Instrum.* **62,** 2639–2645 (1991).
10. R. Turner, A target field approach to optimal coil design. *J. Phys. D.* **19,** L147–151 (1986).
11. T. W. Carlson, K. A. Derby, K. C. Haveryszko, M. Weideman, Design and evaluation of shielded gradient coils. *Magn. Reson. Med.* **26,** 191–206 (1992).
12. H. Liu, L. S. Petropoulos, A spherical gradient coil for ultrafast imaging applications, *in* "Proc., ISMRM, 4th Annual Meeting, New York, 1996," p. 1394.
13. Q. Liu, D. G. Hughes, P. S. Allen, Improved, minimum-inductance, elliptic-cylinder z-gradient coil using axial and azimuthal current flow. *J. Magn. Reson. B.* **113,** 228–235 (1996).
14. J. W. Carlson, M. S. Roos, Shielded gradient coils on hyperbolic surfaces of revolution. *Magn. Reson. Med.* **34,** 762–769 (1995).
15. C. D. Eccles, S. Crozier, W. Roffman, D. M. Doddrell, P. Back, P. T. Callaghan, Practical aspects of shielded gradient-coil design for localized in vivo NMR spectroscopy and small-scale imaging. *Magn. Reson. Imaging* **12,** 621–630 (1994).
16. R. Turner, Gradient coil design: a review of methods. *Magn. Reson. Imaging* **11,** 903–920 (1993).
17. R. Turner, Minimum inductance coils. *J. Phys. E.* **21,** 948–952 (1988).
18. J. D. Jackson, "Classical Electrodynamics," Wiley, New York, 1962.
19. F. B. Hildebrand, "Advanced Calculus for Applications," 2nd ed., Prentice-Hall, NJ, 1976.
20. D. C. Alsop, T. J. Connick, Optimization of torque-balanced asymmetric head gradient coils. *Magn. Reson. Med.* **35,** 875–886 (1996).
21. R. Turner, Electrical coils. US Patent 5,289,151; priority date February 22, 1994.
22. J. R. Reitz, F. J. Milford, R. W. Christy, "Foundations of Electromagnetic Theory," 4th ed., Addison-Wesley, New York, 1989.
23. J. W. Cooley, J. W. Tukey, An algorithm for the machine computation of complex Fourier series. *Math. Comput.* **19,** 297–301 (1965).